Systematic study of the resonancelike structure in the collisional flavor instability of neutrinos

Jiabao Liu,[1] Masamichi Zaizen,[2] and Shoichi Yamada[3,4]

[1]*Department of Physics and Applied Physics, School of Advanced Science and Engineering, Waseda University, Tokyo 169-8555, Japan*
[2]*Faculty of Science and Engineering, Waseda University, Tokyo 169-8555, Japan*
[3]*Department of Physics, School of Advanced Science and Engineering, Waseda University, Tokyo 169-8555, Japan*
[4]*Research Institute for Science and Engineering, Waseda University, Tokyo 169-8555, Japan*

(Received 14 February 2023; accepted 23 May 2023; published 9 June 2023)

Investigations on the resonancelike phenomenon in the collisional flavor instability (CFI) of neutrinos, which were observed in the linear phase recently, are reported. We show that it occurs not only for the isotropy-preserving modes as pointed out in the previous work but also for the isotropy-breaking modes and that it enhances the linear growth rate of the CFI. Employing linear analysis and nonlinear numerical simulations in the two-flavor scheme and under the relaxation approximation for the collision term, we discuss the criterion for the resonancelike phenomenon observed in the linear phase, its effect on the subsequent nonlinear evolution as well as the influences of homogeneity-breaking ($k \neq 0$) perturbations and of anisotropy in the background on the resonancelike structure. We will also touch on idea the cohabitation of the resonancelike structure with the fast-flavor conversion.

DOI: 10.1103/PhysRevD.107.123011

I. INTRODUCTION

Neutrino flavor oscillations, particularly the fast-flavor conversion (FFC), have been studied extensively recently due to their more rapid growth compared to other conversion modes [1–6]. The neutrino-flavor-lepton-number (NFLN) crossing, that is, the situation, in which one flavor is dominant over the other in certain momentum directions while the opposite is true in other directions at least for a pair of neutrino flavors, is known to be the criterion for FFC [7]. In its application to core-collapse supernovae (CCSNe), the electron-lepton-number (ELN) crossing has been conveniently searched for in many papers [8–18], since other flavor-lepton-numbers are normally much smaller. The ordinary nonforward scatterings of neutrinos were once thought to destroy the coherence among neutrinos, thus, working against the neutrino flavor oscillations. The interplay between FFC and ordinary collisions has been investigated from various directions [19–27]. Interestingly, some numerical simulations, in which the collision rate was artificially modified by orders of magnitudes, found that FFC can be enhanced by the collisions [22]. It was also pointed out that the collisions may modify the neutrino spectra so that FFC could be driven [28]. The so-called collisional dilemma, i.e., enhancement or damping of FFC by the ordinary collision, has not been fully resolved so far.

Recently the existence of a new type of flavor conversion referred to as the collisional flavor instability (CFI), which is driven by the collisions themselves and can occur without the NFLN crossing and hence FFC, was pointed out [29]. Properties of CFI were investigated in the same framework in another paper [27]. It was also shown that the onset of CFI could be hastened by FFC [30]. For homogeneous, isotropic, and monochromatic neutrino distributions the condition for CFI is thought to be that the collision rate for neutrino should be different from that for antineutrino [29]. The existence of CFI was later confirmed numerically for homogeneous, isotropic but non-monochromatic neutrino distributions [31]. The authors added to the criterion for CFI a condition that there exists at least one ELN crossing in neutrino energy. The first global simulation of CFI was performed for static backgrounds taken from different stages in a core-collapse supernova simulation [32], demonstrating that the flavor oscillation due to CFI could occur faster than advection. On the other hand, the enhancement of CFI by an asymmetry in the collision rates between neutrino and antineutrino was first noticed in [27]. The resonancelike behavior was pointed out in [33].

In the following sections, we derive the exact linear growth rate of the CFI mode with $k = 0$ in the resonancelike structure based on the dispersion relation for the homogeneous, isotropic and monochromatic neutrino distributions in the background and give the criterion for the resonancelike phenomenon as well. We consider not only the isotropy-preserving mode but also the isotropy-breaking mode, which has been somehow overlooked in the literature so far, and demonstrate that they also give rise to the resonancelike phenomenon. For the isotropy-preserving mode, on the other hand, we solve the quantum kinetic equation numerically in the resonancelike region and study the nonlinear evolution of the system there. We show that the saturation is reached more rapidly in that case but that the saturation level is hardly affected.

We then procced to the non-monochromatic case. We adopt the Fermi-Dirac distribution for the neutrino energy. Numerically evaluating the dispersion relation, we find that the growth rate in and the criterion for the resonancelike phenomenon obtained in the monochromatic case remain good approximations if the monochromatic collision rates are simply replaced by the mean collision rates. Finally, the effect of nonvanishing wave numbers ($k \neq 0$) in the perturbation or of the anisotropy in the background angular distributions in momentum space is studied again based on the dispersion relation. It is found that CFI gets weaker in both cases. We also touch the case, in which the ELN crossing is present initially and the FFC coexists with the resonancelike structure of CFI.

II. DISPERSION RELATION

The neutrino flavor content in the two-flavor approximation is described by the neutrino flavor density matrix

$$\rho(x,P) = \begin{pmatrix} f_{\nu_e} & S \\ S^* & f_{\nu_x} \end{pmatrix}, \tag{1}$$

where the star means the complex conjugate, the diagonal elements are neutrino occupation numbers in the individual flavor eigenstates whereas the off-diagonal elements represent the coherence between the two flavors, $x = (x^\mu)$ is the spacetime position, and $P = (E, \boldsymbol{v})$ is the 4-momentum vector of neutrinos in which neutrinos are assumed to be ultrarelativistic particles traveling at the speed of light $|\boldsymbol{v}| = 1$ in natural units, which we will employ hereafter throughout the paper. We use the signature convention of $\eta_{\mu\nu} = \mathrm{diag}(+1,-1,-1,-1)$ for the Minkowski metric. In the flavor isospin convention, the negative energy $E < 0$ stand for antineutrinos as $\rho(E) = -\bar{\rho}(-E)$. Note that quantities associated with antineutrinos are indicated by the bar.

The evolution of the flavor density matrix is described by the quantum kinetic equation

$$\mathrm{i}v\cdot\partial\rho = [H,\rho] + \mathrm{i}C, \tag{2}$$

where H is the Hamiltonian and C is the collision term. The Hamiltonian has the vacuum, matter and neutrino contributions given as

$$\begin{aligned} H &= H_{\mathrm{vac}} + H_{\mathrm{mat}} + H_\nu, \\ H_{\mathrm{vac}}(x,P) &= \frac{M^2}{2E}, \\ H_{\mathrm{mat}}(x,P) &= \sqrt{2}G_{\mathrm{F}} v\cdot\mathrm{diag}(j_e(x), j_x(x)), \\ H_\nu(x,P) &= \sqrt{2}G_{\mathrm{F}} v\cdot\int \mathrm{d}P'\rho(x,P')v', \end{aligned} \tag{3}$$

where M^2 is the neutrino mass-squared matrix; $j_\alpha(x)$ is the lepton number 4-current of the charged lepton species α; the integral over 4-momentum is abbreviated as

$$\int dP = \int_{-\infty}^{\infty}\frac{E^2dE}{2\pi^2}\int\frac{d\boldsymbol{v}}{4\pi}. \tag{4}$$

The collision term C can be written for neutrinos in the relaxation approximation as

$$C(x,P) = \frac{1}{2}\{\mathrm{diag}(\Gamma_e(x,P),\Gamma_x(x,P)), \rho_{\mathrm{eq}} - \rho\}, \tag{5}$$

where the curly bracket denotes the anticommutator, $\Gamma_\alpha(x,P)$ is the collision rate for the charged lepton α, and ρ_{eq} is the density matrix for the equilibrium state that is approached through the collision. The collision term for antineutrinos is written in the same manner.

The quantum kinetic equation (2) may be linearized with respect to S if $|S| \ll f_i$ as

$$\begin{aligned} & v\cdot(\partial - \Lambda_{0e} + \Lambda_{0x})S_{ex} \\ & \quad + (f_{\nu_e} - f_{\nu_x})\sqrt{2}G_{\mathrm{F}}\int \mathrm{d}P' v\cdot v' S_{ex}(P') \\ & \quad + \frac{1}{2E}\sum_{z=e,x}(M^2_{ez}S_{zx} - S_{ez}M^2_{zx}) + \mathrm{i}\Gamma_{ex}S_{ex} = 0, \end{aligned} \tag{6}$$

where $\Lambda_{0z} = \sqrt{2}G_{\mathrm{F}}[j_z(x) + \int \mathrm{d}P f_{\nu_z}(x,P)v]$ and $\Gamma_{ex}(E) = [\Gamma_e(E) + \Gamma_x(E)]/2$. Assuming the plane wave solution as usual as

$$S(x,P) = S(k,P)e^{\mathrm{i}k\cdot x}, \tag{7}$$

where $k = (\omega, \boldsymbol{k})$ is the 4-wave vector and ignoring the vacuum term, which is important for the slow instabilities [34] but plays a minor role to give initial perturbations for the fast instability, we obtain

$$\{v\cdot(k - \Lambda_{0e} + \Lambda_{0x}) + \mathrm{i}\Gamma_{ex}\}S_{ex} + (f_{\nu_e} - f_{\nu_x})v\cdot a = 0, \tag{8}$$

where the vector a is defined as

$$a = \sqrt{2}G_{\rm F}\int {\rm d}P S_{ex}(P)v. \tag{9}$$

Then, S can be solved as

$$S_{ex}(k,P) = -\frac{(f_{\nu_e} - f_{\nu_x})v\cdot a}{v\cdot(k-\Lambda_{0e}+\Lambda_{0x})+{\rm i}\Gamma_{ex}}. \tag{10}$$

Substitution of this expression back into the definition of a in Eq. (9) leads to the following homogeneous equation:

$$\Pi_{ex}(k)a_{ex}(k) = 0, \tag{11}$$

where the matrix Π_{ex} is defined as

$$\Pi_{ex}(k) = \eta + \sqrt{2}G_{\rm F}\int \frac{{\rm d}P(f_{\nu_e} - f_{\nu_x})v\otimes v^{\mathsf{T}}}{v\cdot(k-\Lambda_{0e}+\Lambda_{0x})+{\rm i}\Gamma_{ex}}. \tag{12}$$

Λ's in the denominator may be absorbed into k, shifting the real part of k alone and unaffecting the instability [35]. Note that the so-called zero mode with $k = 0$ does not mean a mode homogeneous in space after this shift. In the isotropic case the neutrino contribution to the shift vanishes.

Nontrivial solutions of a exist if and only if

$$\det\Pi_{ex}(k) = 0, \tag{13}$$

which gives us the dispersion relation $\omega = \omega(\boldsymbol{k})$. The positive imaginary part of ω, ${\rm Im}\omega > 0$, implies that the flavor eigenstate is unstable and the perturbation in S grows exponentially in time—an indication of CFI. Introducing spherical coordinates for the neutrino velocity $\boldsymbol{v}$, we can write down the matrix Π_{ex} as

$$\Pi_{ex}(k) = \eta + \sqrt{2}G_{\rm F}\int_{-\infty}^{\infty}\frac{E^2{\rm d}E}{2\pi^2}\int_{-1}^{1}\frac{{\rm d}c_\theta}{2}\int_0^{2\pi}\frac{{\rm d}\phi}{2\pi}\frac{f_{\nu_e}(E,\boldsymbol{v}) - f_{\nu_x}(E,\boldsymbol{v})}{\omega - \boldsymbol{v}\cdot\boldsymbol{k} + {\rm i}\Gamma_{ex}(E)}$$
$$\times\begin{pmatrix} 1 & \sqrt{1-c_\theta^2}c_\phi & \sqrt{1-c_\theta^2}s_\phi & c_\theta \\ \sqrt{1-c_\theta^2}c_\phi & (1-c_\theta^2)c_\phi^2 & (1-c_\theta^2)s_\phi c_\phi & \sqrt{1-c_\theta^2}c_\theta c_\phi \\ \sqrt{1-c_\theta^2}s_\phi & (1-c_\theta^2)s_\phi c_\phi & (1-c_\theta^2)s_\phi^2 & \sqrt{1-c_\theta^2}c_\theta s_\phi \\ c_\theta & \sqrt{1-c_\theta^2}c_\theta c_\phi & \sqrt{1-c_\theta^2}c_\theta s_\phi & c_\theta^2 \end{pmatrix}, \tag{14}$$

where the following abbreviations are used: $c_\theta = \cos(\theta)$; $s_\theta = \sin(\theta)$; $c_\phi = \cos(\phi)$; $s_\phi = \sin(\phi)$.

The expression is significantly simplified if the background neutrino is isotropic in momentum space. In fact, for $k = 0$, Π_{ex} becomes even simpler, being diagonal. The equation to be solved is reduced in this case to

$$I = \sqrt{2}G_{\rm F}\int_{-\infty}^{\infty}\frac{E^2{\rm d}E}{2\pi^2}\frac{f_{\nu_e}(E) - f_{\nu_x}(E)}{\omega + {\rm i}\Gamma_{ex}(E)} = -1, 3. \tag{15}$$

Note that the solutions for $I = 3$ are degenerate with the multiplicity of 3. The solutions of Eq. (15) are collectively referred to as the homogeneity-preserving modes although the wave vector is shifted. It should be noted that only the solution branch for $I = -1$ has been studied in previous papers [31,33]. This is because the authors of these papers assumed tacitly that the perturbation is isotropic. In fact, the spatial components of a vanish in that case so that the three spatial components of Eq. (11) become trivial. This is equivalent to ignoring the modes for $I = 3$. If one allows anisotropic perturbations instead, the spatial components of a become nonzero and the solution branch for $I = 3$ is recovered. For this reason, we call the solution branch for $I = -1$ the isotropy-preserving branch and refer to the solution for $I = 3$ as the isotropy-breaking branch.

The analysis of the real and imaginary parts of Eq. (15) leads to the necessary condition for the occurrence of CFI, i.e., ${\rm Im}[\omega] > 0$, that the following function, $F(E)$, of $E(>0)$,

$$\begin{aligned} F(E) = {} & [f_{\nu_e}(E) - f_{\nu_x}(E)][{\rm Im}\omega + \Gamma_{ex}(E)] \\ & \times[({\rm Re}\omega)^2 + ({\rm Im}\omega + \bar{\Gamma}_{ex}(E))^2] \\ & - [f_{\bar{\nu}_e}(E) - f_{\bar{\nu}_x}(E)][{\rm Im}\omega + \bar{\Gamma}_{ex}(E)] \\ & \times[({\rm Re}\omega)^2 + ({\rm Im}\omega + \Gamma_{ex}(E))^2] \end{aligned} \tag{16}$$

should have at least one zero point, or crossing in energy. When the energy-dependent collision rates, $\Gamma_{ex}(E)$ and $\bar{\Gamma}_{ex}(E)$, are identical for neutrinos and antineutrinos, this condition is reduced to the criterion derived in Ref. [31].

III. MONOCHROMATIC NEUTRINOS

A. Exact solutions in linear analysis

In this section, we consider monochromatic neutrinos and solve Eq. (15) analytically. We assume the following

background distributions:

$$f_{\nu_e}(E)-f_{\nu_x}(E)=\frac{2\pi^2}{\sqrt{2}G_{\rm F}E^2}[\mathfrak{g}\delta(E-\epsilon)-\bar{\mathfrak{g}}\delta(E+\bar{\epsilon})], \quad (17)$$

where $\mathfrak{g},\bar{\mathfrak{g}},\epsilon,\overline{\epsilon},$ are model parameters. Then Eq. (15) becomes

$$\frac{\mathfrak{g}}{\omega+{\rm i}\Gamma}-\frac{\bar{\mathfrak{g}}}{\omega+{\rm i}\bar{\Gamma}}=-1,3, \quad (18)$$

where $\Gamma=\Gamma_{ex}(E=\epsilon),\bar{\Gamma}=\bar{\Gamma}_{ex}(E=-\bar{\epsilon})$. Note that in the typical situation in the supernova core of our concern following inequalities hold by several orders of magnitude: $\mathfrak{g},\bar{\mathfrak{g}}\gg\Gamma,\bar{\Gamma}$, the fact used in the following. Equation (18) can be solved easily to produce

$$\omega_\pm=-A-{\rm i}\gamma\pm\sqrt{A^2-\alpha^2+{\rm i}2G\alpha}, \quad (19)$$

for the isotropy-preserving modes and

$$\omega_\pm=\frac{A}{3}-{\rm i}\gamma\pm\sqrt{\left(\frac{A}{3}\right)^2-\alpha^2-{\rm i}\frac{2}{3}G\alpha}, \quad (20)$$

for the isotropy-breaking modes. In the above equations, the following notations are introduced:

$$G=\frac{\mathfrak{g}+\bar{\mathfrak{g}}}{2},\quad A=\frac{\mathfrak{g}-\bar{\mathfrak{g}}}{2},\quad \gamma=\frac{\Gamma+\bar{\Gamma}}{2},\quad \alpha=\frac{\Gamma-\bar{\Gamma}}{2}. \quad (21)$$

Note that when the collision rates are identical between neutrino and antineutrino, or $\alpha=0$, the imaginary part of $\omega_\pm$ is $-\gamma<0$, implying that they are all stable. It follows hence that the inequality of the collision rates is needed for CFI, which was the criterion postulated in Ref. [29].

The complex frequencies given in Eqs. (19) and (20) are approximated as

$$\omega_\pm=\begin{cases}-A-{\rm i}\gamma\pm\left(|A|+{\rm i}\frac{G|\alpha|}{|A|}\right), & \text{if } A^2\gg G|\alpha|,\\ -A-{\rm i}\gamma\pm\sqrt{{\rm i}2G\alpha}, & \text{if } A^2\ll G|\alpha|,\end{cases} \quad (22)$$

for the isotropy-preserving branch and

$$\omega_\pm=\begin{cases}A-{\rm i}\gamma\pm\left(\frac{|A|}{3}-{\rm i}\frac{1}{3}\frac{G|\alpha|}{|A|}\right), & \text{if } A^2\gg G|\alpha|,\\ \frac{A}{3}-{\rm i}\gamma\pm\sqrt{-{\rm i}\frac{2}{3}G\alpha}, & \text{if } A^2\ll G|\alpha|,\end{cases} \quad (23)$$

for the isotropy-breaking branch. The results for the isotropy-preserving modes were derived previously outside the resonancelike region in [29,31] and inside it in [33], whereas those for the isotropy-breaking modes have not been presented so far because the authors assumed isotropy not only for the background but also for perturbations as we mentioned earlier.

We plot the real and imaginary parts of ω for the two branches in Figs. 1 and 2, respectively, for the following parameter values: $\mathfrak{g}=1\ {\rm cm}^{-1},\gamma=2.05\times10^{-7}\ {\rm cm}^{-1}$, $\alpha=-4.5\times10^{-8}\ {\rm cm}^{-1}$. In these plots we take $\bar{\mathfrak{g}}$ as a free parameter. It is apparent from the plots of imaginary part that there is a rather narrow region of $\bar{g}$, in which the growth rate is enhanced roughly by two orders of magnitude. This is the resonancelike structure that Ref. [33] first pointed out and we will focus on in this paper. In fact, the resonancelike peak occurs near the point, at which the real parts of ω_+ and ω_- come close to each other. Note that although the resonancelike structure was reported only for the isotropy-preserving modes in Ref. [33], it occurs also for the isotropy-breaking modes as shown in Fig. 2.

To locate where the enhancement occurs exactly, we differentiate $\omega_+(\mathfrak{g},\bar{\mathfrak{g}},\Gamma,\bar{\Gamma})$ of the isotropy-preserving branch in Eq. (19) with respect to $\bar{\mathfrak{g}}$ as

$$\begin{aligned}\frac{\partial\omega}{\partial\bar{g}}&=\frac{1}{2}+\frac{1}{2}(A^2-\alpha^2+{\rm i}2G\alpha)^{-\frac{1}{2}}(-A+{\rm i}\alpha)\\&=\frac{1}{2}+\frac{1}{2}|C|^{-\frac{1}{2}}\left[\left(-A\cos\frac{\theta[C]}{2}+\alpha\sin\frac{\theta[C]}{2}\right)\right.\\&\quad\left.+{\rm i}\left(\alpha\cos\frac{\theta[C]}{2}-A\sin\frac{\theta[C]}{2}\right)\right],\end{aligned} \quad (24)$$

where we define C as

$$C=A^2-\alpha^2+{\rm i}2G\alpha=|C|e^{{\rm i}\theta[C]}. \quad (25)$$

The imaginary part of the derivative vanishes at the unique value of $\bar{\mathfrak{g}}$ that corresponds to $A^2=\alpha^2$. Thus, the resonancelike peak occurs when $|A|\approx|\alpha|$, i.e., the number densities of neutrino and antineutrino come close to each other. Note that the difference between Γ and $\bar{\Gamma}$ is usually orders of magnitude smaller than the difference between g and $\bar{g}$, i.e., $|\alpha|\ll|A|$.

In the isotropy-preserving branch, the imaginary part of ω_+ is given approximately as

$${\rm Im}\omega_+\approx\begin{cases}-\gamma+\frac{G|\alpha|}{|A|}, & \text{if } A^2\gg G|\alpha|,\\ -\gamma+\sqrt{G|\alpha|}, & \text{if } A^2\ll G|\alpha|,\end{cases} \quad (26)$$

In the situation of our concern, where $\mathfrak{g},\bar{\mathfrak{g}}\gg\Gamma,\bar{\Gamma}$, the first case is nonresonant, since $G\gg|\alpha|$. On the other hand, the second case may fall in the resonancelike region. Note that the imaginary part is positive in the second regime unless α is much smaller than γ. In the first regime, on the other hand, the signature of the imaginary part is determined by the competition of the difference between g and $\bar{g}$ and of that between Γ and $\bar{\Gamma}$.

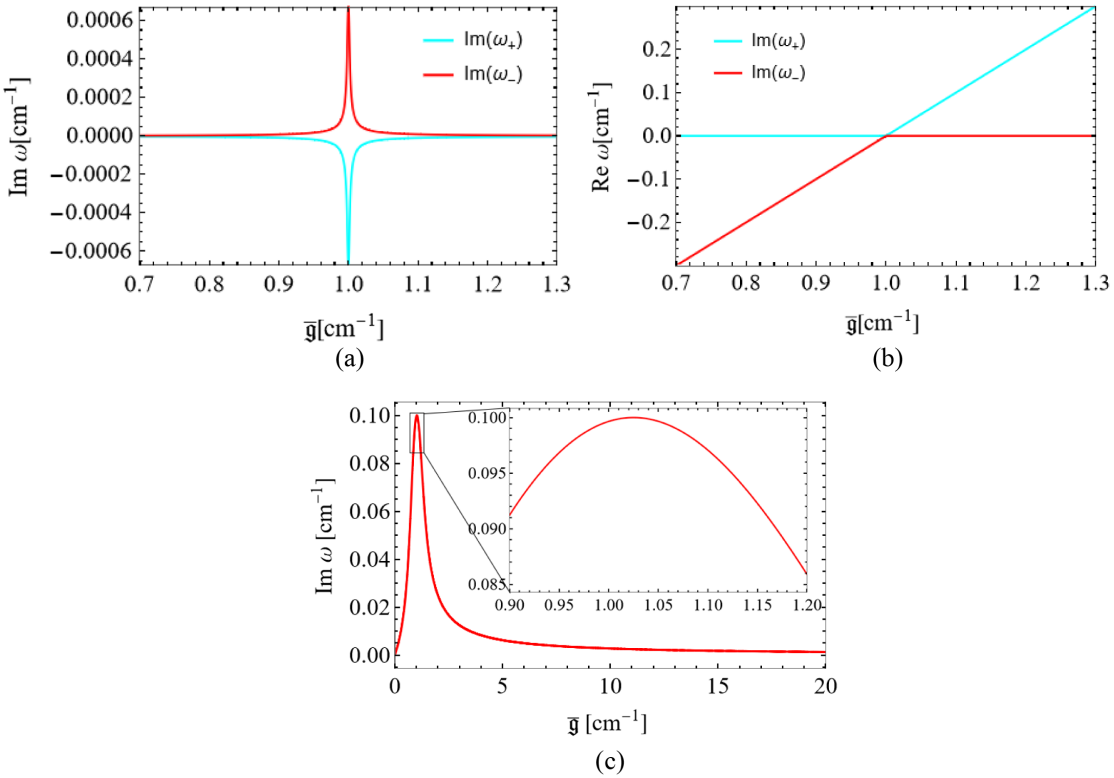

FIG. 1. Real and imaginary parts of the complex frequency ω for the isotropy-preserving branch as a function of $\bar{\mathfrak{g}}$. For (a) and (b) we take $\mathfrak{g} = 1\ \mathrm{cm}^{-1}$, $\gamma = 2.05 \times 10^{-7}\ \mathrm{cm}^{-1}$, $\alpha = -4.5 \times 10^{-8}\ \mathrm{cm}^{-1}$, whereas for (c) we artificially magnify the collision rate of antineutrinos to $\bar{\Gamma} = 2.5 \times 10^{-2}\ \mathrm{cm}^{-1}$, so that $|\alpha| \sim 2.5 \times 10^{-2}\ \mathrm{cm}^{-1}$ which implies $\bar{\mathfrak{g}} \approx 1.025\ \mathrm{cm}^{-1}$ at the resonancelike peak. See the text for the notational details.

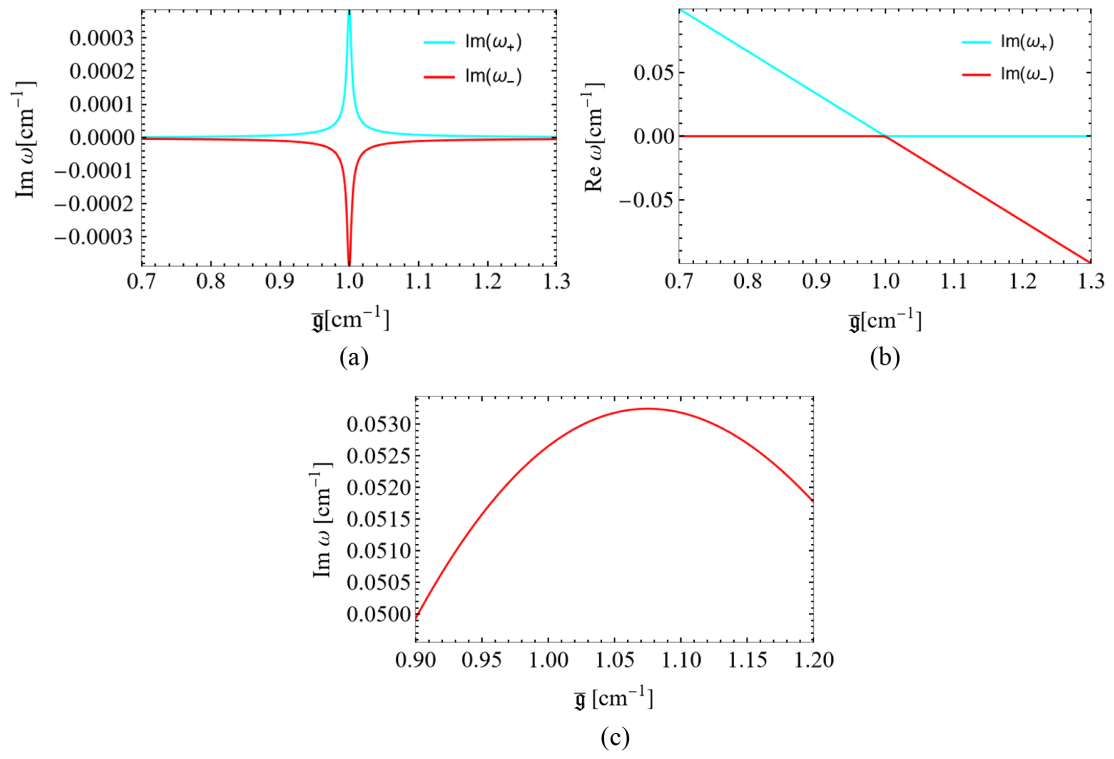

FIG. 2. Same as Fig. 1 but for the isotropy-breaking branch.

Although we have so far regarded ω as a function of $\bar{\mathfrak{g}}$, one can also take other parameters. If one varies $\mathfrak{g}$ instead of $\bar{\mathfrak{g}}$, the same criterion $|A| \approx |\alpha|$ is obtained. This resonancelike peak, if regarded as a function of one of the collision rates, reaches its maximum height at a certain value of this rate. Note also that the resonancelike peak occurs at $\mathfrak{g} \sim \bar{\mathfrak{g}}$ but not exactly at $\mathfrak{g} = \bar{\mathfrak{g}}$. To see this more clearly, we choose a different parameter set, in which we artificially raise the collision rate of antineutrinos to an unrealistically high value $\bar{\Gamma} = 0.025\ \mathrm{cm}^{-1}$ so that $|\alpha| \approx 0.025\ \mathrm{cm}^{-1}$. We then obtain $\bar{\mathfrak{g}} \approx 1.025\ \mathrm{cm}^{-1}$ at the peak. This deviation from $\mathfrak{g} = 1\ \mathrm{cm}^{-1}$ is confirmed in Fig. 1(c). One should also notice that the peak amplitude in the resonancelike structure is much larger, and the peak width is also much broader in this extreme case. A similar analysis shows that the resonancelike structure occurs also for the isotropy-breaking branch. The peak location is a bit different from that for the isotropy-preserving mode and satisfies $A^2 = (3\alpha)^2$, as demonstrated in Fig. 2(c) again for the exaggerated value of $\bar{\Gamma} = 0.025\ \mathrm{cm}^{-1}$. It is also observed that the peak width in the resonancelike structure for the isotropy-breaking mode is not appreciably different from that for the isotropy-preserving mode whereas the peak amplitude is smaller by a factor ~ 2 for the isotropy-breaking mode than that for the isotropy-preserving mode.

So far we have employed the dispersion relation. The behavior discussed above can be also derived directly from the original quantum kinetic equation. Since it provides a different insight into the resonancelike structure, we will look at it below. We assume that the background is homogeneous, isotropic, and monochromatic. The vacuum and matter terms are ignored to focus on CFI. Then the Hamiltonian and the collision term are given as

$$H = H_\nu = H_\mathrm{d} + H_\mathrm{o} = \begin{pmatrix} \mathfrak{g}_{\nu_e} - \mathfrak{g}_{\bar{\nu}_e} & 0 \\ 0 & \mathfrak{g}_{\nu_x} - \mathfrak{g}_{\bar{\nu}_x} \end{pmatrix} + \begin{pmatrix} 0 & S - \bar{S} \\ S^* - \bar{S}^* & 0 \end{pmatrix}, \tag{27}$$

$$C = \begin{pmatrix} \Gamma_e(\mathfrak{g}_{\nu_e,eq} - \mathfrak{g}_{\nu_e}) & \frac{\Gamma_e+\Gamma_x}{2}(S_{eq} - S) \\ \frac{\Gamma_e+\Gamma_x}{2}(S^*_{eq} - S^*) & \Gamma_x(\mathfrak{g}_{\nu_x,eq} - \mathfrak{g}_{\nu_x}) \end{pmatrix},$$
$$\bar{C} = \begin{pmatrix} \bar{\Gamma}_e(\mathfrak{g}_{\bar{\nu}_e,eq} - \mathfrak{g}_{\bar{\nu}_e}) & \frac{\bar{\Gamma}_e+\bar{\Gamma}_x}{2}(\bar{S}_{eq} - \bar{S}) \\ \frac{\bar{\Gamma}_e+\bar{\Gamma}_x}{2}(\bar{S}^*_{eq} - \bar{S}^*) & \bar{\Gamma}_x(\mathfrak{g}_{\bar{\nu}_x,eq} - \mathfrak{g}_{\bar{\nu}_x}) \end{pmatrix}. \tag{28}$$

Note that the Hamiltonian is divided into the diagonal part H_d and the off-diagonal part H_o. The equilibrium distributions are set to the unperturbed states:

$$\mathfrak{g}_{\nu_i,\mathrm{eq}} = \mathfrak{g}_{\nu_i}, \quad \mathfrak{g}_{\bar{\nu}_i,\mathrm{eq}} = \mathfrak{g}_{\bar{\nu}_i}, \quad \bar{S}^{(*)}_\mathrm{eq} = S^{(*)}_\mathrm{eq} = 0. \tag{29}$$

The linearized equations for S and $\bar{S}$ are given as

$$\mathrm{i}\partial_t \boldsymbol{V} = \boldsymbol{W}\boldsymbol{V}, \tag{30}$$

where $\boldsymbol{V}$ is vector defined as

$$\boldsymbol{V} = \begin{pmatrix} S \\ \bar{S} \end{pmatrix}, \tag{31}$$

and $\boldsymbol{W}$ is the matrix expressed as

$$\begin{pmatrix} -(\mathfrak{g}_{\bar{\nu}_e} - \mathfrak{g}_{\bar{\nu}_x}) - \mathrm{i}\frac{1}{2}(\Gamma_e + \Gamma_x) & (\mathfrak{g}_{\nu_e} - \mathfrak{g}_{\nu_x}) \\ -(\mathfrak{g}_{\bar{\nu}_e} - \mathfrak{g}_{\bar{\nu}_x}) & (\mathfrak{g}_{\nu_e} - \mathfrak{g}_{\nu_x}) - \mathrm{i}\frac{1}{2}(\bar{\Gamma}_e + \bar{\Gamma}_x) \end{pmatrix}. \tag{32}$$

Note that we assume that the perturbation is also isotropic in deriving these equations here.

The general solution is given as the superposition of two independent solutions:

$$\boldsymbol{V}(t) = \boldsymbol{V}_+ e^{-\mathrm{i}\omega_+ t} + \boldsymbol{V}_- e^{-\mathrm{i}\omega_- t}, \tag{33}$$

where $\boldsymbol{V}_\pm, \omega_\pm$ are the eigenvectors and eigenvalues to the matrix W. The eigenvalues are obtained as [31]

$$\omega_\pm = -A - \mathrm{i}\gamma \pm \sqrt{A^2 - \alpha^2 + 2\mathrm{i}G\alpha}, \tag{34}$$

where the notations are identical to those for Eq. (19).

It is interesting to point out that the elimination of the diagonal part of the Hamiltonian does not change the two eigenvalues, which suggests that CFI is driven by an interplay of the off-diagonal part of the Hamiltonian and the collision terms. That may be illuminated more clearly by treating the collision term as a perturbation. Let us first consider the case with $H = H_\mathrm{o}$ and no collision term, $C = 0$. The eigenvalues and eigenvectors in this case are given as

$$\omega_1 = 0, \qquad \boldsymbol{V}_1 = \begin{pmatrix} 1 \\ 1 \end{pmatrix},$$
$$\omega_2 = -\mathfrak{g} - \bar{\mathfrak{g}}, \qquad \boldsymbol{V}_2 = \begin{pmatrix} \mathfrak{g} \\ \bar{\mathfrak{g}} \end{pmatrix}. \tag{35}$$

Below we introduce the following notations:

$$\mathfrak{g} = \mathfrak{g}_{\nu_e} - \mathfrak{g}_{\nu_x}, \qquad \bar{\mathfrak{g}} = \mathfrak{g}_{\bar{\nu}_e} - \mathfrak{g}_{\bar{\nu}_x},$$
$$\Gamma = \frac{1}{2}(\Gamma_e + \Gamma_x), \qquad \bar{\Gamma} = \frac{1}{2}(\bar{\Gamma}_e + \bar{\Gamma}_x), \tag{36}$$

This is a stable-flavor evolution with no growth of amplitudes.

Now we reinstate the collision terms but as a perturbation. The characteristic equation is then written as

$$[-\mathfrak{g} - (\omega_0 + \Delta\omega) - i\Gamma][\bar{\mathfrak{g}} - (\omega_0 + \Delta\omega) - i\bar{\Gamma}] + \mathfrak{g}\bar{\mathfrak{g}} = 0, \tag{37}$$

where the eigenvalue is expressed as the sum of the unperturbed value given in Eq. (35) and a (small) shift. To linear order, the shifts are obtained for the two modes as

$$\Delta\omega_1 \approx \frac{i\bar{\mathfrak{g}}\Gamma - i\mathfrak{g}\bar{\Gamma}}{\mathfrak{g} - \bar{\mathfrak{g}}},$$
$$\Delta\omega_2 \approx \frac{i\mathfrak{g}\Gamma - i\bar{\mathfrak{g}}\bar{\Gamma}}{\bar{\mathfrak{g}} - \mathfrak{g}}. \tag{38}$$

They are divergent at $\mathfrak{g} = \bar{\mathfrak{g}}$ unless $\Gamma = \bar{\Gamma}$, an indication of the resonancelike structure in the current setting, i.e., the collision term is assumed to be small and so is the shift, the latter of which is no longer correct at $g \approx \bar{g}$, however. Note that the two shifts have opposite signatures, in qualitative agreement with the exact solution.

B. Numerical simulations

Now we go beyond the linear analysis. We solve the quantum kinetic equation

$$i\partial_t\rho = [H_\nu, \rho] + iC \tag{39}$$

for the homogeneous, isotropic, and monochromatic neutrino distributions. The vacuum and matter terms are omitted again. The following simulations are meant to study the nonlinear evolution of the isotropy-preserving mode both outside and inside the resonancelike regions. For this purpose we vary, rather arbitrarily, $\bar{\mathfrak{g}}$, the distribution function of antineutrino. For comparison, we also run linear simulations in which the Hamiltonian is fixed to the initial value.

Since the vacuum term, which would produce perturbations to the flavor eigenstate automatically, is neglected here, we give an initial perturbation by hand as follows:

$$\mathfrak{g} = \mathfrak{g}_{\nu_e} = 1\ \mathrm{cm}^{-1},$$
$$\bar{\mathfrak{g}} = \mathfrak{g}_{\bar{\nu}_e} \text{ is a free variable},$$
$$S = \bar{S} = 10^{-8} + 0i\ \mathrm{cm}^{-1}. \tag{40}$$

For simplicity, we assume that all neutrinos are initially in the electron flavor and the initial perturbation is isotropic so that the isotropy-breaking mode does not appear in this simulation. As discussed in the previous section, the occurence of CFI is dictated by the four quantities: $\mathfrak{g}, \bar{\mathfrak{g}}, \Gamma$, and $\bar{\Gamma}$ [see Eq. (36)]. Note that in the linear simulations, $\mathfrak{g}$ and $\bar{\mathfrak{g}}$ are conserved quantities and unchanged in time.

The collision rates are chosen as

$$\Gamma_e = \Gamma_x = \frac{\Gamma}{2} = 1.6 \times 10^{-7}\ \mathrm{cm}^{-1},$$
$$\bar{\Gamma}_e = \bar{\Gamma}_x = \frac{\bar{\Gamma}}{2} = 2.5 \times 10^{-7}\ \mathrm{cm}^{-1}, \tag{41}$$

which correspond to

$$\gamma = 2.05 \times 10^{-7}\ \mathrm{cm}^{-1},$$
$$\alpha = -4.5 \times 10^{-8}\ \mathrm{cm}^{-1}. \tag{42}$$

Since the Γ and $\bar{\Gamma}$ are much smaller than $\mathfrak{g}$ and $\bar{\mathfrak{g}}$, the resonancelike peak occurs essentially at $\mathfrak{g} = \bar{\mathfrak{g}}$.

The results of the linear simulations are shown first in Fig. 3 for three different values of $\bar{\mathfrak{g}}$: 1.000, 1.009, and 1.100 cm^{-1}. The first one almost corresponds to the resonancelike peak whereas the second and third values give the edge of and a point outside the resonancelike region, respectively. The blue curves are the modulus of flavor coherence, $|S|$, plotted against time while the yellow lines indicate, for comparison, the exponential growths with the values of ω_+ given in Eq. (19) for these settings. As should be clear, $|S|$ shows the exponential growth as expected in all cases. In particular, the growth is much faster indeed in the resonancelike region. Note also that the initial conditions are not exactly the eigenmodes corresponding to ω_+ and some deviations from the exact exponential growth are seen.

Now we procced to the results of the fully nonlinear simulations run for the first two initial conditions employed in the linear simulations presented just above. They correspond to the peak and edge of the resonancelike structure, respectively. In Fig. 4 we plot not only $|S|$, the modulus of the flavor coherence and the off-diagonal component of the density matrix, but also the distribution functions of all neutrinos, which are also the diagonal components of the density matrix, as functions of time. For reference, the exponential growths with the values of ω_+ in Eq. (19) for the current settings are again exhibited.

One recognizes clearly that there are two distinct phases, the linear phase, in which the flavor coherence grows exponentially at the rate given in the linear analysis, and the nonlinear saturation phase, where the $|S|$ peaks out and levels off thereafter. The distribution functions of neutrinos and antineutrinos also settle gradually to states that are steady in the statistical sense and are different from the initial ones (see the insets in each panel). The transition from the linear phase to the nonlinear phase may be characterized by $|S| \sim \mathfrak{g}$. It is found from the result in the resonancelike structure that the saturation level of the flavor coherence is not particularly large (actually smaller) compared with the case for the edge of the resonancelike region and that the role of resonancelike phenomenon is just to shorten the time it takes to reach saturation.

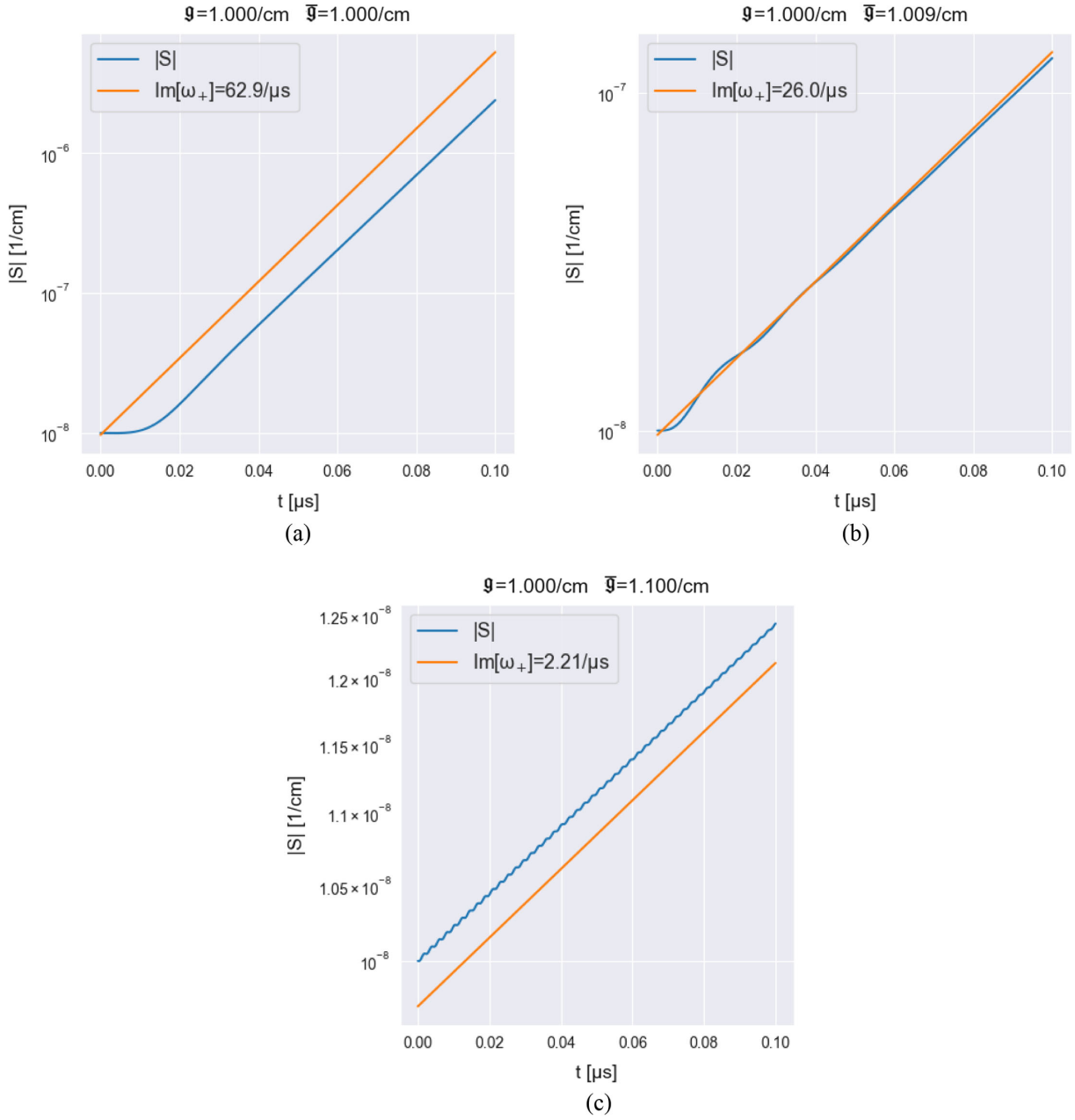

FIG. 3. The time evolutions of $|S|$, the modulus of the flavor coherence, for three values of $\bar{\mathfrak{g}}$ in the linear simulations. We take $\alpha = -4.5 \times 10^{-8}$ cm^{-1}, and $\mathfrak{g} = 1$ cm^{-1}. In the plots, the yellow straight lines are the exponential evolution at the growth rate, and the blue curves are numerical results. (a) $\bar{\mathfrak{g}} = 1.000$ cm^{-1} approoximately corresponds to the resonancelike peak, (b) $\bar{\mathfrak{g}} = 1.009$ cm^{-1} gives a an edge of the resonancelike region, and (c) $\bar{\mathfrak{g}} = 1.100$ cm^{-1} is outside the resonancelike region.

This may be supported by another simulation, a variant of the second case, in which the $\bar{\Gamma}$ is changed to 3.6×10^{-7} cm^{-1} with other parameters, particularly $\mathfrak{g}$ and $\bar{\mathfrak{g}}$, fixed so that it should give the point closer to the resonancelike peak. The result is presented as Fig. 4(c). Note that the linear growth rate is twice as large as that in the second case and is close to that in the first case. The saturation occurs earlier consistently with the enhanced linear growth rate. On the other hand, the asymptotic state is almost the same as that in the second case. It is mostly determined by the initial neutrino distributions and little affected by the resonancelike phenomenon.

It should be noted that the asymptotic state may be oscillating in time and is steady—not in the literal sense but in the statistical sense. The substantially smaller populations of ν_x and $\bar{\nu}_x$ in the asymptotic states in these models are the consequence of our choice of the equilibrium state in the relaxation approximation adopted in the simulation and are rather artificial. It should be also be mentioned that in reality, where the background matter and neutrinos

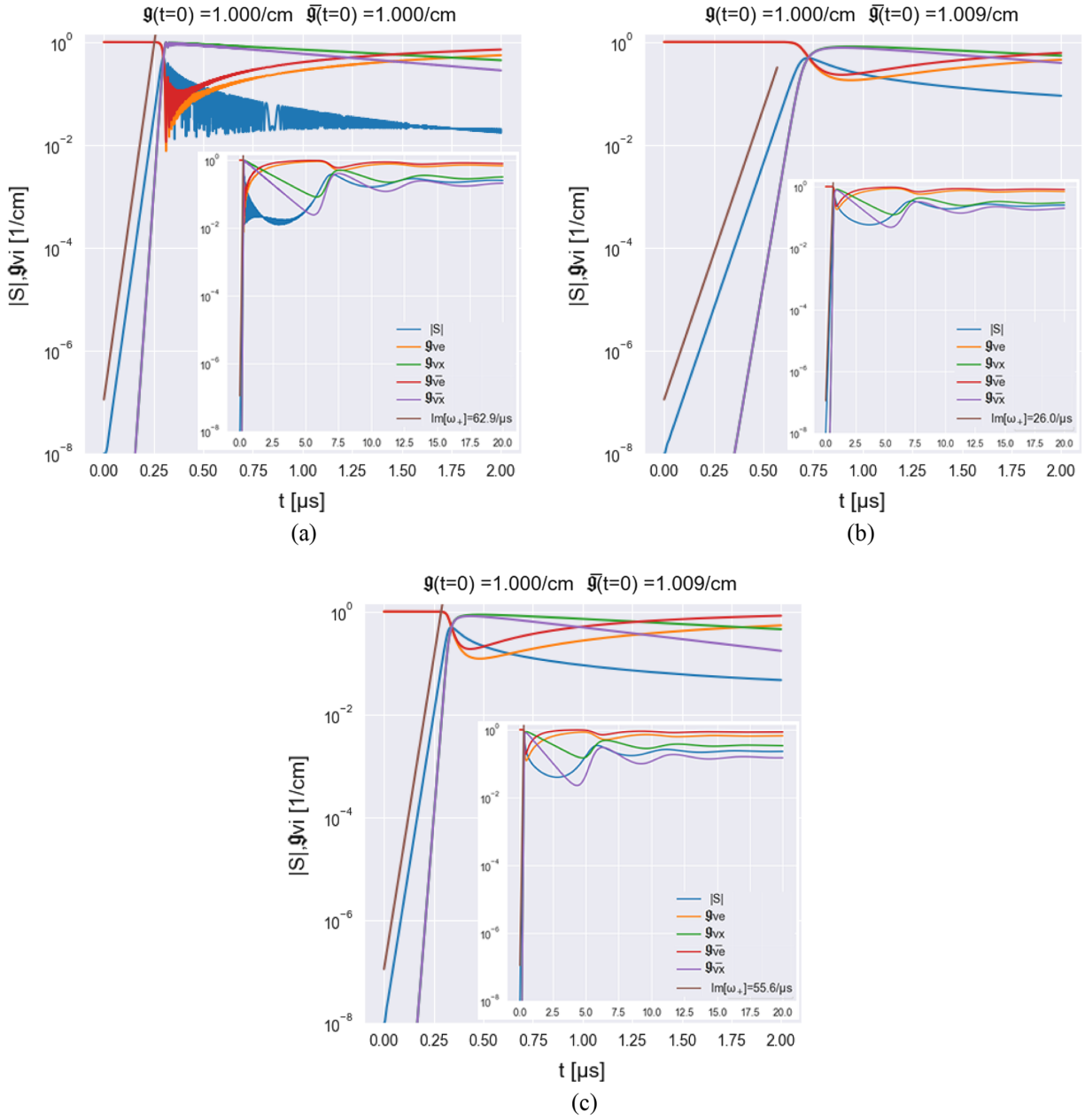

FIG. 4. (a) and (b) the nonlinear time evolutions for the same initial conditions as in Figs. 3(a) and 3(b), respectively. Not only the flavor coherence $|S|$ (blue lines) but also the distribution functions of neutrinos and antineutrinos (colors indicated in the legends) are presented. (c) a variant of (b), in which $\bar{\Gamma}$ is changed to 3.6×10^{-7} cm^{-1} so that the initial condition should be closer to the resonancelike peak. The longer evolutions leading up to the asymptotic states are shown in the insets.

themselves may change significantly due to advection over the timescale of neutrino oscillations, the asymptotic state may never be reached. It was found that CFI could win the competition against advection (see [32]). What consequences the accelerated saturation may have, if any, for the core-collapse supernova remain to be studied.

It is interesting to point out that in the first case corresponding approximately to the resonancelike peak, a very fast-flavor bouncing occurs in the beginning of the nonlinear saturation phase right after the peak-out. It is due to the diagonal part of the collision term, in which the equilibrium distributions is imposed. In fact, if we reset the equilibrium values to the actual asymptotic values when the nonlinear phase is reached, this feature disappears.

IV. NONMONOCHROMATIC NEUTRINOS

We extend the analyses in the previous section to nonmonochromatic neutrinos. We assume that neutrinos and antineutrinos have energy spectra given by the Fermi-Dirac

distributions. We begin with the linear analysis and discuss the criterion for the resonancelike phenomenon as well as the growth rate at the resonancelike peak in this case. We then study the nonlinear evolutions of the system in the resonancelike region for the isotropy-preserving mode with $k = 0$ by numerical simulations. Finally, going back to the linear analysis, we investigate the effects of nonvanishing wave numbers in the perturbation as well as of anisotropies in the background on CFI. As an extreme case of the latter, we discuss a possible interplay of the resonancelike structure in CFI with FFC on the same footing.

A. Linear analysis

We assume that neutrinos and antineutrinos have continuous energy spectra given by the Fermi-Dirac distributions,

$$f_i(E, g_i, T_i, \mu_i) = \frac{g_i}{\exp[E/T_i - \mu_i] + 1}, \tag{43}$$

where g_i, T_i, and μ_i are the model parameters for the neutrino species i, and E is the neutrino energy. Assuming for simplicity that only electron flavor is present initially, we choose

$$\begin{aligned} &g_{\nu_e} = 1, \\ &g_{\bar{\nu}_e} \text{ is a free variable}, \\ &g_{\nu_x} = g_{\bar{\nu}_x} = 0, \end{aligned} \tag{44}$$

and the shorthand notation

$$\begin{aligned} g &= g_{\nu_e}, \\ \bar{g} &= g_{\bar{\nu}_e}, \end{aligned} \tag{45}$$

will be used in the following. The temperatures are set to

$$\begin{aligned} T_{\nu_e} &= 4 \text{ MeV}, \\ T_{\bar{\nu}_e} &= 5 \text{ MeV}, \end{aligned} \tag{46}$$

and we further assume that $\mu = 0$. Although it is not presented here, we confirmed that a nonzero μ does not qualitatively change the result in the following. The collision term is now assumed to depend on the energy quadratically as

$$\Gamma(E) = \Gamma_0 \left(\frac{E}{10 \text{ MeV}} \right)^2, \tag{47}$$

with

$$\Gamma_0 = 10^{-5} \text{ cm}^{-1} \tag{48}$$

common to all flavors.

For later convenience we introduce the number density multiplied by $\sqrt{2}G_F$, n_i, the mean energy, $\langle E \rangle_i$, and the mean collision rate, $\langle \Gamma \rangle_i$ for the neutrino species i as

$$\begin{aligned} n_i &= \sqrt{2} G_F \int \frac{E^2 dE}{2\pi^2} f(E, g_i, T_i, \mu_i), \\ \langle E \rangle_i &= \frac{\sqrt{2} G_F}{n_i} \int \frac{E^3 dE}{2\pi^2} f(E, g_i, T_i, \mu_i), \\ \langle \Gamma \rangle_i &= \frac{\sqrt{2} G_F}{n_i} \int \frac{E^2 dE}{2\pi^2} \Gamma(E) f(E, g_i, T_i, \mu_i). \end{aligned} \tag{49}$$

These three quantities defined above have same unit. Note that a change in g_i influences only n_i while a variation in T_i or μ_i influences all of n_i, $\langle E \rangle_i$, and $\langle \Gamma \rangle_i$. We also introduce the following quantities:

$$\begin{aligned} G &= \frac{n + \bar{n}}{2}, \qquad A = \frac{n - \bar{n}}{2}, \\ \gamma &= \frac{\langle \Gamma \rangle + \langle \bar{\Gamma} \rangle}{2}, \qquad \alpha = \frac{\langle \Gamma \rangle - \langle \bar{\Gamma} \rangle}{2}. \end{aligned} \tag{50}$$

We solve Eq. (15) numerically to obtain the dispersion relation. In doing so, the energy range from 0 MeV to 80 MeV is divided into nonuniform 128 bins concentrated more at low energies.

We plot in Fig. 5 the contour lines for $\mathrm{Re}I = -1$ or 3 (blue) and $\mathrm{Im}I = 0$ (orange) in the complex ω plane for some representative values of $\bar{g}$. The intersection of the two contour lines gives the dispersion relation $\omega(k)$ at $k = 0$. One of the two solutions (except for the origin) with a positive imaginary part is the unstable mode. The first three plots in the figure are for the isotropy-preserving branch at $\bar{g} = 0.51, 0.511, 0.512$, respectively, and the last plot is for the isotropy-breaking branch at $\bar{g} = 0.512$. For the current choice of parameters, which correspond to

$$\begin{aligned} \langle \Gamma \rangle &= 2.07031 \times 10^{-6} \text{ cm}^{-1}, \\ \langle \bar{\Gamma} \rangle &= 3.23531 \times 10^{-6} \text{ cm}^{-1}, \\ \alpha &= \frac{\langle \Gamma \rangle - \langle \bar{\Gamma} \rangle}{2} \approx -5.825 \times 10^{-7} \text{ cm}^{-1}, \end{aligned} \tag{51}$$

the resonancelike peak is expected to occur approximately at $\bar{g} = 0.512$ [panels (c) and (d)] giving $n \approx \bar{n} \approx 4.88691 \text{ cm}^{-1}$. This is confirmed in Fig. 6, where we plot the real and imaginary parts of ω for the unstable isotropy-preserving branch as a function of $\bar{g}$. One can see a familiar enhancement of the imaginary part, or the growth rate of the instability.

We also investigate an extreme case, in which we artificially magnify the collision rate $\bar{\Gamma}$ of antineutrino by five orders of magnitude, $\Gamma_0 = 1 \text{ cm}^{-1}$ in Eq. (48), while the other parameters are unchanged. This gives $\alpha = -1.6174 \text{ cm}^{-1}$. The result is shown in Fig. 6(c). The resonancelike peak occurs at $\bar{g} = 0.74$, which

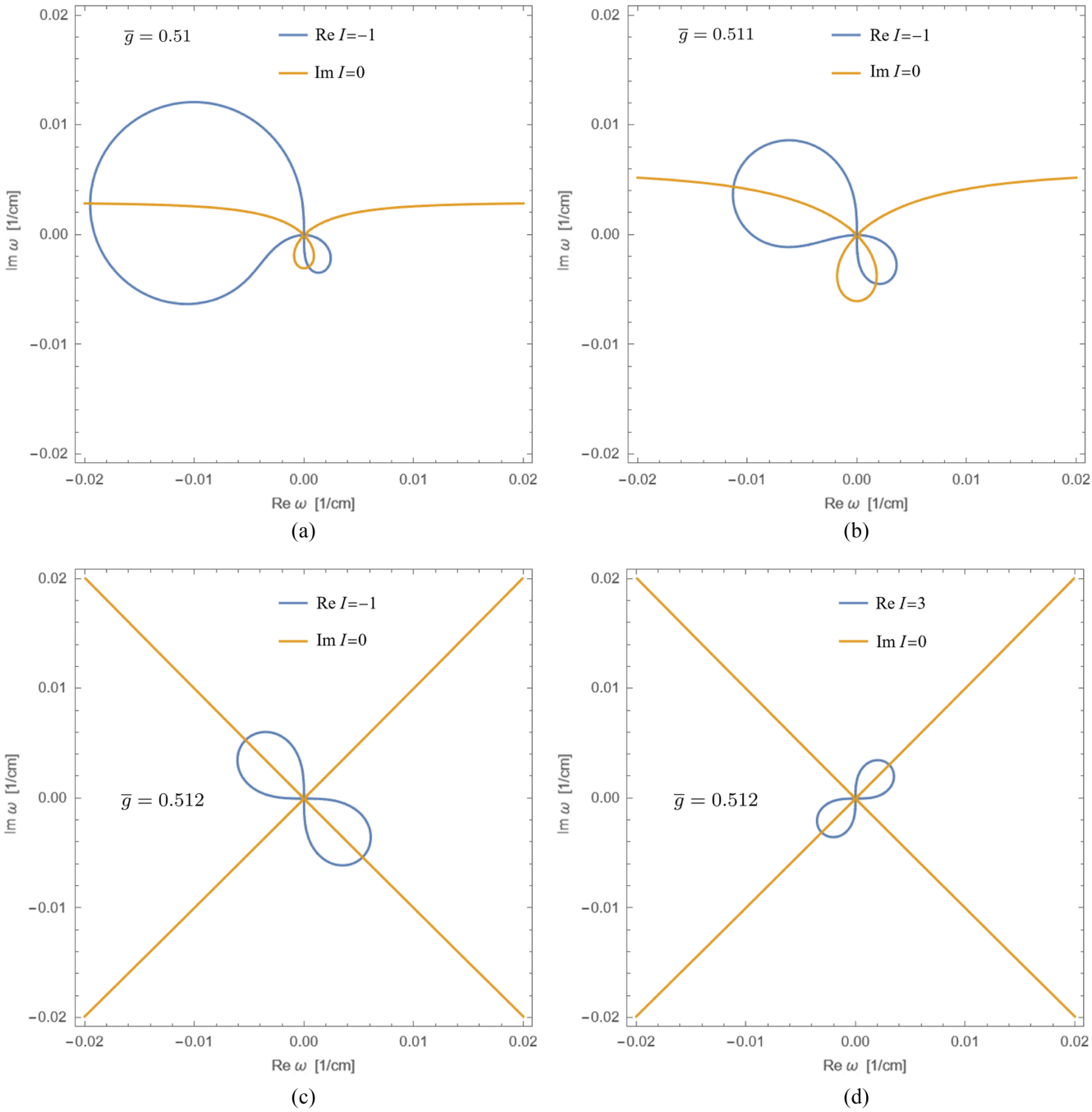

FIG. 5. The contour lines for Re$I = -1$ or 3 (blue) and Im$I = 0$ (orange) in Eq. (15). Their intersections give the dispersion relation $\omega(k = 0)$. Panels (a)–(c) are for the isotropy-preserving branch whereas panel (d) displays the result for the isotropy-breaking branch.

corresponds to $A = -1.0081\ \mathrm{cm}^{-1}$. The number density of antineutrino is noticably different from that of neutrino in this case just as inferred from the result of the monochromatic case. Again the approximate formula (orange line) is compared with the numerical result shown in blue. This time the approximation is not so successful as before although the peak shift as well as the broadening of resonancelike region are captured qualitatively. It is pointed out that thanks to this broadening the case with $n = \bar{n}$ is still in the resonancelike region, although not at the peak, and hence the growth rate is enhanced. We explored other neutrino spectra, such as the Fermi-Dirac distributions with nonvanishing chemical potentials or Gaussian and polynomial distributions that are not too irregular. The results are qualitatively the same as those given above and hence will not be presented here.

Finally, it is worth pointing out that the growth rate of the resonancelike structure is well-approximated by the

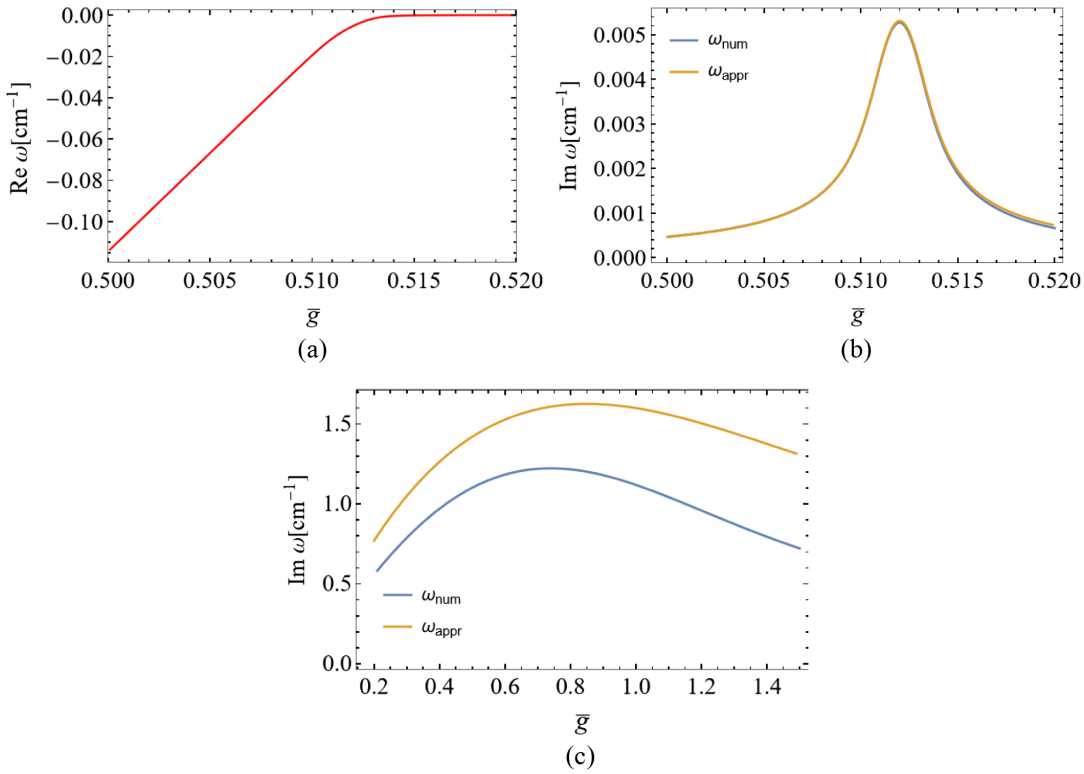

FIG. 6. The real (a) and imaginary (b) parts of the complex frequency ω for the unstable isotropy-preserving branch as a function of $\bar{g}$. For the imaginary part, the numerical solution $\mathrm{Im}\omega_{\mathrm{num}}(\bar{g})$ shown in blue is compared with the approximate one $\mathrm{Im}\omega_{\mathrm{appr}}(\bar{g})$ exhibited in orange. In panel (c), the collision rate $\bar{\Gamma}$ of antineutrinos is artificially magnified by 10^5.

formula for the monochromatic case, Eq. (19), for ω_+, with the following substitutions:

$$\begin{aligned} \overset{(-)}{g} &\to \overset{(-)}{n} \\ \overset{(-)}{\Gamma} &\to \overset{(-)}{\langle\Gamma\rangle}. \end{aligned} \tag{52}$$

Note that this approximate formula agrees with the one derived previously in [33] under the assumption of $|\Gamma|, |\bar{\Gamma}| \ll |\omega|$ if γ and α^2 are neglected accordingly. This is demonstrated in Fig. 6(b), where the numerical solution displayed in blue is compared with the approximate one presented in orange. Their agreement matches what was shown in [33]. Although the criterion for resonancelike phenomenon posited in that paper is appropriate only when the collision rates are small, the condition $|A| \sim |\alpha|$ is always satisfied at the resonancelike peak regardless of the parameter values.

B. Numerical simulations

We again solve Eq. (39) numerically for homogeneous and isotropic neutrinos with Fermi-Dirac distributions as the energy spectra. The background distributions are actually the same as those employed for the linear analysis in the previous section, Eqs. (44)–(48). Since the vacuum term is omitted in the kinetic equation, we need to set an initial perturbation by hand, which is also assumed to be isotropic and homogeneous. Hence only the isotropy-preserving branch is considered. We take $\bar{g}$ as a free parameter and vary it so that the unperturbed state should be either near the resonancelike peak or near the edge of the resonancelike region.

In the simulation, the energy range from 1 MeV to 100 MeV is divided uniformly into 100 bins this time. We adopt the following initial perturbations only to the off-diagonal components of the density matrix:

$$\begin{aligned} S(E) &= (1 + 0.8\mathrm{i})10^{-5} f(E), \\ \bar{S}(E) &= (-0.5 + \mathrm{i})10^{-5} \bar{f}(E). \end{aligned} \tag{53}$$

The numbers in the functions are chosen rather arbitrarily.

The results of the linear simulations, in which the Hamiltonian is fixed to the initial value, is shown in Fig. 7 for two choices of $\bar{g}$; one corresponding approximately to the resonancelike peak and the other giving the edge of the resonancelike region. The value of A/α measures how close the initial configuration is to the resonancelike peak; the closer to unity it is, the nearer to the resonancelike peak the initial state is. It is evident that the flavor coherence grows at a common rate for all energies [31],

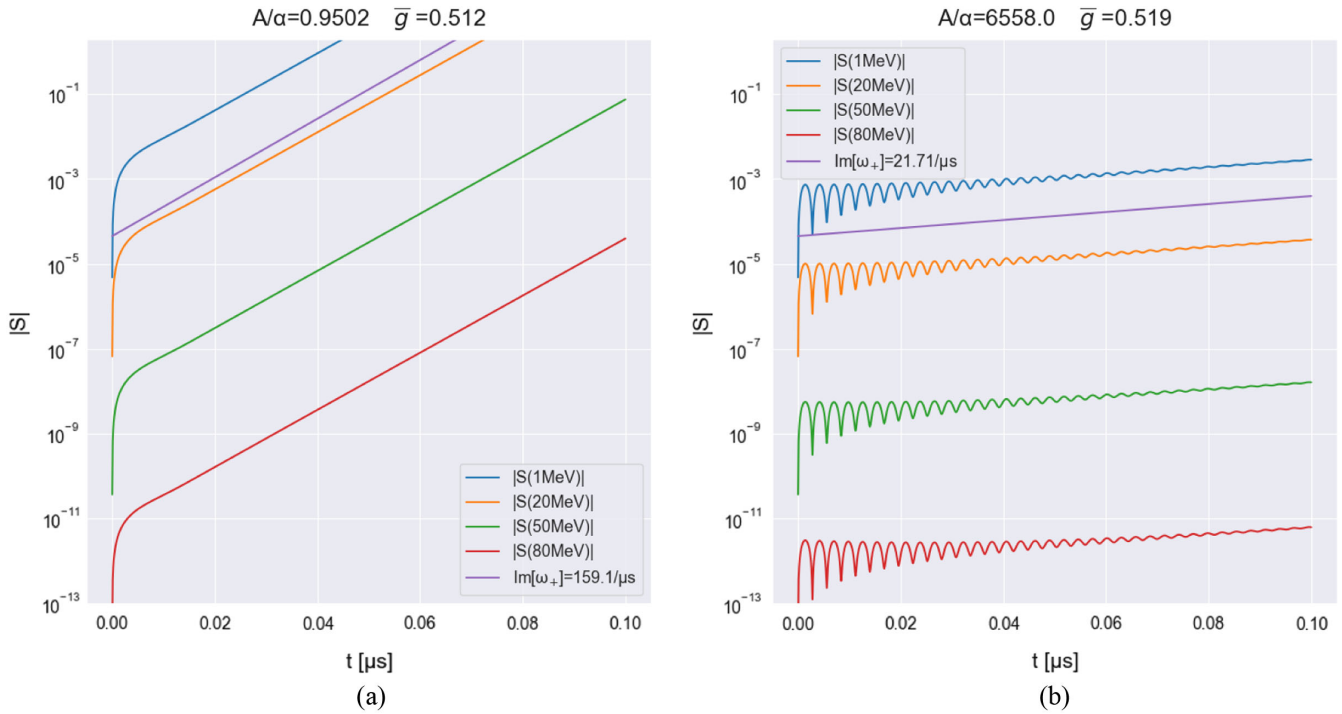

FIG. 7. The time evolutions of $|S|$, the modulus of the flavor coherence, at different neutrino energies in the linear simulations for the continuous energy spectrum. Two values of $\bar{g}$ are adopted: $\bar{g} = 0.512$ and 0.519; $\alpha = -1.165 \times 10^{-6}$ cm^{-1}, and $g = 1$ giving $n_{\nu_e} = 4,887$ cm^{-1}. The violet lines indicate for reference the exponential evolution at the growth rate given by the linear analysis.

just as expected from the energy-independent nature of $\omega(k)$. In the resonancelike region, it grows much faster.

The corresponding results for the nonlinear simulations are presented in Figs. 8 and 9. Again one recognizes that the linear phase is followed by the nonlinear saturation phase also in this case with the nonmonochromatic energy spectra. In the linear phase the flavor coherence grows at a common rate for all energies just as in the linear simulations given above (see Fig. 8). In the case for the resonancelike peak [panel (a)], the nonlinear phase is reached much faster than in the case for the edge of the resonancelike region [panel (b)].

It is also found that the beginning of the nonlinear phase is marked for each energy when $|S(E)| = f(E)$ is satisfied individually, which is a direct extension of the monochromatic case. The saturation level is not much different between the two cases (see Fig. 9), indicating again that the main effect of the resonancelike phenomenon is to accelerate the linear growth and the asymptotic state is hardly affected. The bouncing in the nonlinear phase is observed only for the resonancelike peak. The bouncing amplitude seems to be related with the difference between the equilibrium distribution and the asymptotic distribution although the exact mechanism of bouncing is not clear at the moment. This is induced by the diagonal part of the collision term. In fact, if we discard the diagonal part effectively by resetting the equilibrium distributions to the asymptotic ones, the bouncing feature is gone just as in the monochromatic case.

C. $k \neq 0$ perturbation/anisotropy in the background

In this last section, we investigate the resonancelike structure either for $k \neq 0$ perturbations in the homogeneous and isotropic background or for $k = 0$ modes in the homogeneous but anisotropic background. We work on the dispersion relations in the linear regime. The neutrino energy spectra are again assumed to be the Fermi-Dirac distributions given in Eq. (43), with the same parameters as in Eqs. (44)–(46) and, in addition, with $\bar{g} = g_{\bar{\nu}_e} = 0.512$, corresponding to the resonancelike peak at $k = 0$. The collision rates are given by Eqs. (47) and (48).

We begin with the $k \neq 0$ perturbation in the homogeneous and isotropic background. In the following the wave vector $\boldsymbol{k}$ is assumed to be parallel to the z-axis. We solve Eq. (14) numerically to obtain the dispersion relation. For $k \neq 0$, there appear two nonvanishing off-diagonal components in Π_{ex} in addition to the diagonal ones, which survive in the $k \to 0$ limit. In order to see how the isotropy-preserving and isotropy-breaking branches at $k = 0$ are mixed with each other to new modes in the $k \neq 0$ case, we decompose Π_{ex} as

$$\Pi^{\mu\nu}_{ex} = \eta^{\mu\nu} + A^{\mu\nu}. \tag{54}$$

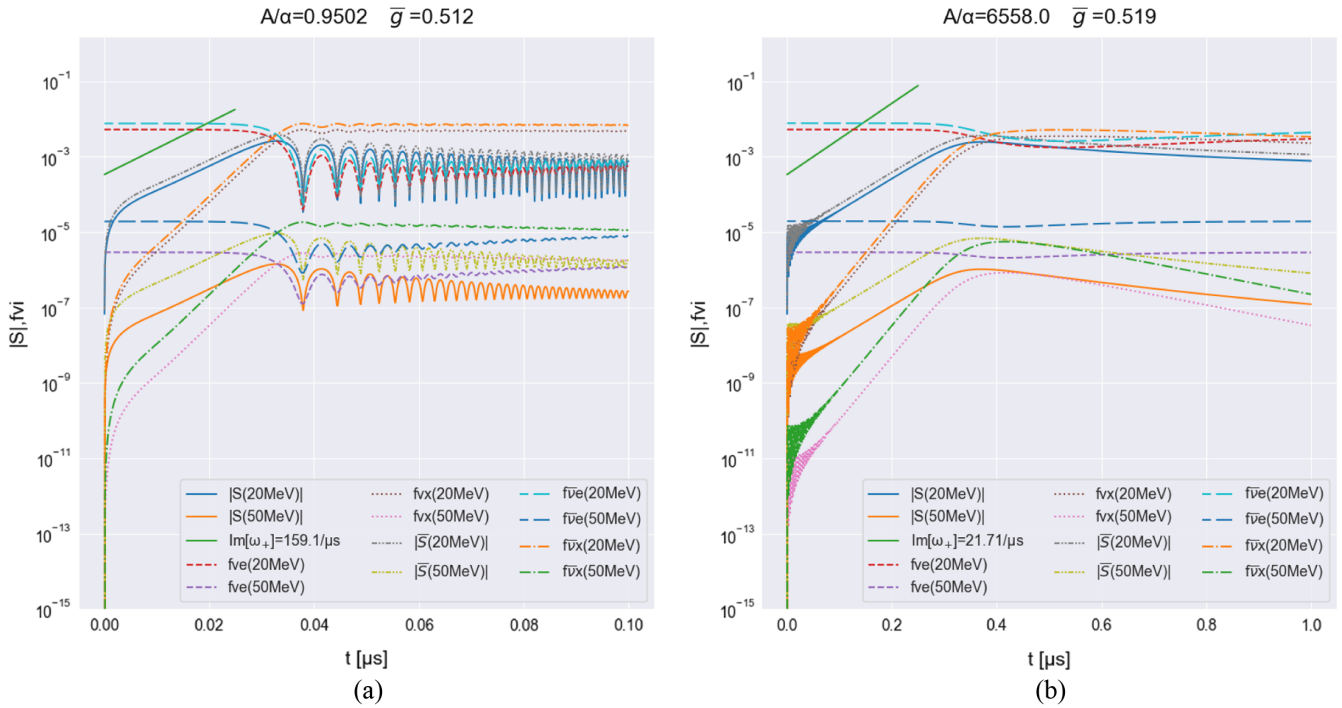

FIG. 8. The nonlinear time evolutions for the same initial conditions as in Fig. 7. Not only the flavor coherence $|S|$ but also the distribution functions of neutrinos and antineutrinos are presented for different energies (line types given in the legend). The purple solid line indicates the exponential growth at the rate given by the linear analysis.

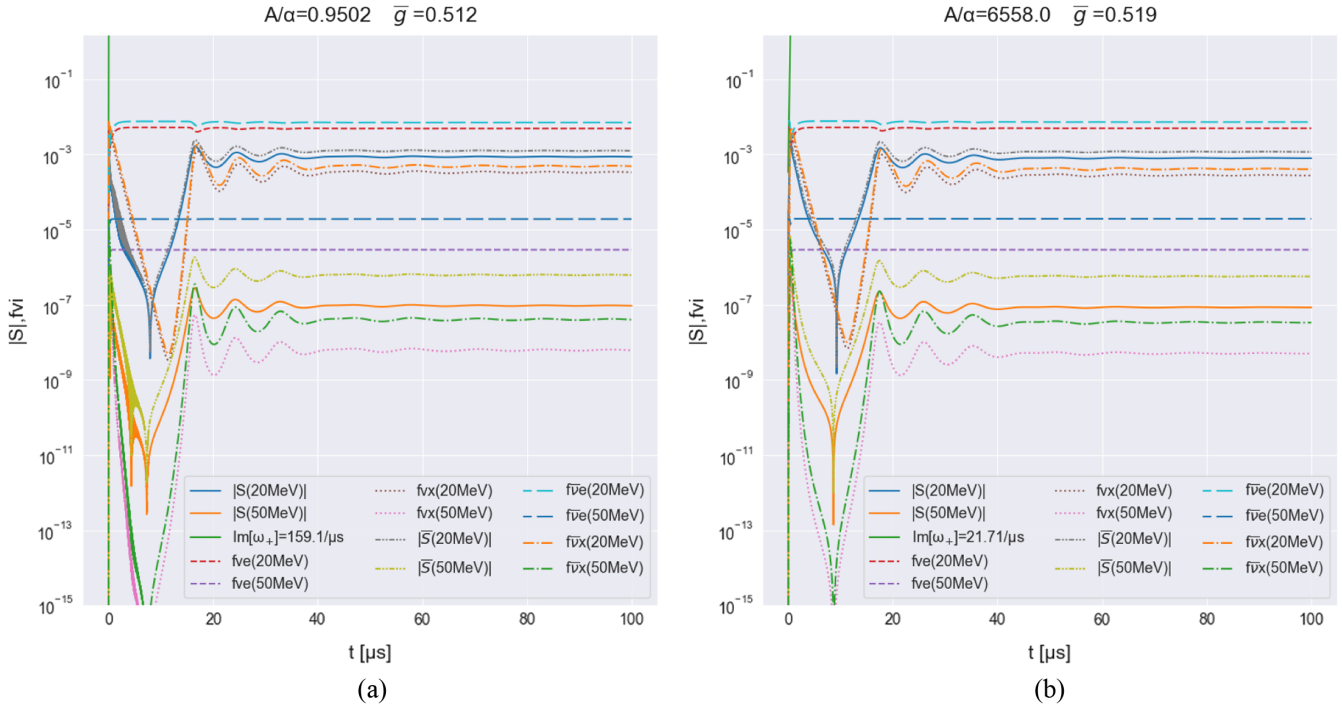

FIG. 9. The longer-term evolutions of the same simulations as in Fig. 8.

Then, its determinant can be written explicitly in a simple form as

$$\det \Pi_{ex} = (A^{11} - 1)^2[(A^{00} + 1)(A^{33} - 1) - (A^{03})^2], \quad (55)$$

where the following relations

$$A^{11} = A^{22},$$
$$A^{30} = A^{03}, \quad (56)$$

are used. Note that in the limit of $k = 0$, the following relations hold further:

$$A^{30} = A^{03} = 0,$$
$$A^{33} = A^{11} = A^{22}, \quad (57)$$

and the dispersion relation is obtained from

$$\det \Pi_{ex} = (A^{00} + 1)(A^{11} - 1)^3 = 0. \quad (58)$$

In fact, the isotropy-preserving branch is derived from the first factor and the isotropy-breaking branch is originated from the second factor. In the case of $k \neq 0$, while $A^{11} - 1 = 0$ is unchanged, $(A^{00}+1)(A^{11}-1)-(A^{03})^2=0$ now mixes the isotropy-preserving and isotropy-breaking branches to produce four branches in general. In the following we look into these modes in detail.

From the first factor in Eq. (55), a pair of solutions are obtained, which take the following form $a = (0, a_x, a_y, 0)$ and are perpendicular to $\boldsymbol{k}$, and they hence break the isotropy in the $x - y$ plane. On the other hand, the second factor can vanish in three different manners: $(1)A^{00} + 1 = A^{03} = 0$, $(2)A^{33} - 1 = A^{03} = 0$, or $(3)(A^{00}+1)(A^{33}-1) = (A^{03})^2 \neq 0$. The first case produces a solution of the form $a = (a_t, 0, 0, 0)$, which is isotropy-preserving. The second case leads to $a = (0, 0, 0, a_z)$, which is hence isotropy-breaking in the z direction; that is, the direction of $\boldsymbol{k}$. The last one yields a solution with the form of $a = (a_t, 0, 0, a_z)$ in general, which is also isotropy-breaking. If the first and second factors vanish simultaneously, the solution takes a combined form; for example, the combination of the first factor with case (1) for the second factor gives a solution of the following form: $a = (a_t, a_x, a_y, 0)$. These cases are exceptional, though, and occur only for special spectra/collision rates. In fact, we find that case (3) is always satisfied in the second factor of Eq. (55) for the ranges of k and $\bar{g}$ considered in this paper.

In Fig. 10, we display plots of the contours indicated in each panel for $k = 0.001$ cm^{-1}. The left panel gives the solutions for the first factor in Eq. (55) whereas the right panel shows the solutions for the second factor. The latter corresponds to case (3) as mentioned above. At this small k, all the modes are not much different from the counterparts at $k = 0$. For later convenience, we refer to the solutions for unstable modes in these plots as Q, W, and Y. Mode Q originated from the first factor in Eq. (55) merges at $k = 0$ with Y from the second factor to give the isotropy-breaking modes. On the other hand, mode W is reduced to the isotropy-preserving mode at $k = 0$. These modes are all isotropy-breaking at $k \neq 0$. In Fig. 11 we plot the linear

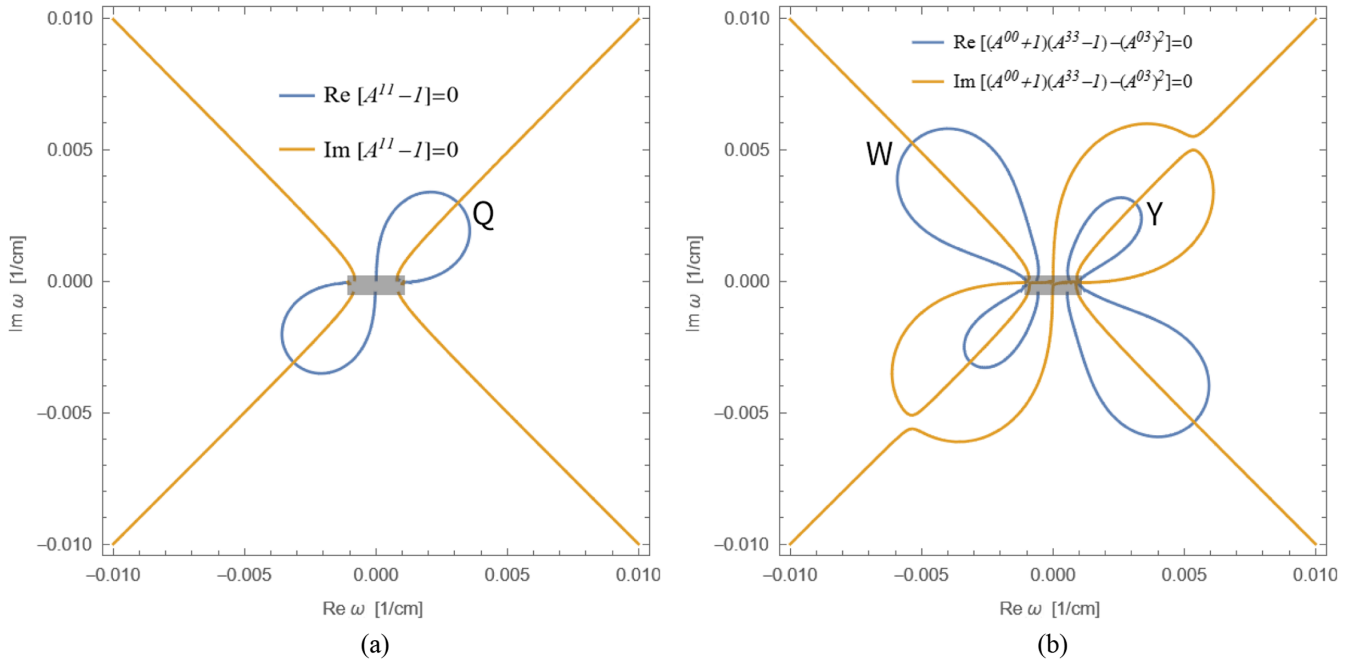

FIG. 10. The plots of the contour lines denoted in each panel in the complex ω plane at $k = 0.001$ cm^{-1}. The gray band around the origin is the numerical unreliable region that should be discarded.

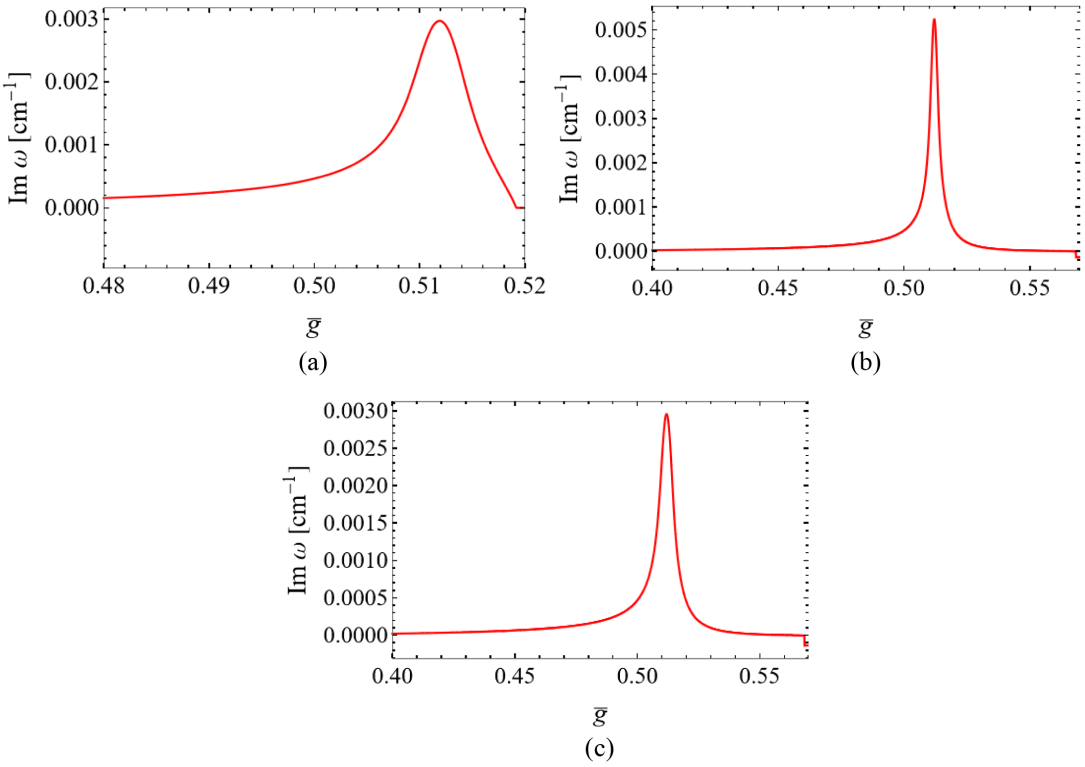

FIG. 11. The resonancelike structures for the unstable branches Q in (a), W in (b), and Y in (c), at $k = 0.001$ cm^{-1}.

growth rates, Imω, for these three modes as a function of $\bar{g}$ at the same value of $k = 0.001$ cm^{-1}. The resonancelike structure is evident in all cases around $\bar{g} = 0.512$.

In Fig. 12, we show the k-dependence of these growth rates at $\bar{g} = 0.512$, i.e., around the resonancelike peak. It is apparent that they decrease monotonically with k, indicating that the resonancelike peak gets weaker at nonvanishing k for all modes. This is actually true outside the resonancelike region as well. The nonzero k tends to reduce the CFI itself. It is noted that the presence of $\boldsymbol{k}$ in the denominator of Eq. (14) poses a challenge in the numerical integration by discretization in the region $-k < \mathrm{Re}\omega < k, 0 < \mathrm{Im}\omega < \Gamma(E_{\mathrm{max}})$. We do not think that the numerical solutions in these ranges are reliable and hence do not consider those solutions outside the resonancelike region or inside it but at large values of k that approach this problematic region, which is indicated as the gray bands around the origin in Fig. 10.

Next we study the effect of the anisotropy in the homogeneous neutrino background on the resonancelike structure. We introduce the following angular-dependence to the neutrino distributions in momentum space:

$$f_i(E, g_i, T_i, \mu_i, \theta, \delta_i) = (1 + \delta_i \cos\theta) f_i(E, g_i, T_i, \mu_i), \qquad (59)$$

where $f_i(E, g_i, T_i, \mu_i)$ on the right hand side is the Fermi-Dirac distribution for neutrino species i; $0 < \theta < \pi$ is the angle that the neutrino velocity makes with the radially outward direction; the factor δ_i controls the degree of anisotropy. Since we are interested in the resonancelike structure in CFI in this paper, we first consider a case with no angular crossing, and hence no FFC. We then look at two cases with different angular crossings to see the interplay between the resonance-like structure in CFI and FFC. We solve Eq. (14) numerically for $k = 0$ to obtain the dispersion relation $\omega(k = 0)$ for the anisotropic (but homogeneous) background just described. Note that the integration over the solid angle can be done analytically for $k = 0$.

We first present the results for the first case, in which only electron-type neutrinos and antineutrinos are present initially with the same anisotropy, $\delta = \bar{\delta}$. We choose the model parameters as in Eqs. (44)–(48) together with $\bar{g} = 0.512$ and $k = 0$ so that the unperturbed state corresponds to the resonancelike peak at $\delta = 0$. We vary the value of δ to see how the anisotropy affects CFI in the resonancelike region. The choice of $k = 0$ simplifies the analysis a lot. In fact, only Π^{03}_{ex}, which is linear in δ, is nonvanishing as the off-diagonal components of Π_{ex} just as in the previous case with $k \neq 0$, and the diagonal components are unchanged from those for the isotropic case. Since the dispersion relation is obtained from $\det \Pi_{ex} = 0$ given as Eq. (55) again, we refer to the corresponding modes as Q, W, and Y. Under the current setting, all modes are isotropy-breaking for $\delta \neq 0$. Note that mode Q is independent of δ and $\bar{\delta}$ in this setting, and is always identical to the isotropy-breaking mode for isotropic neutrinos.

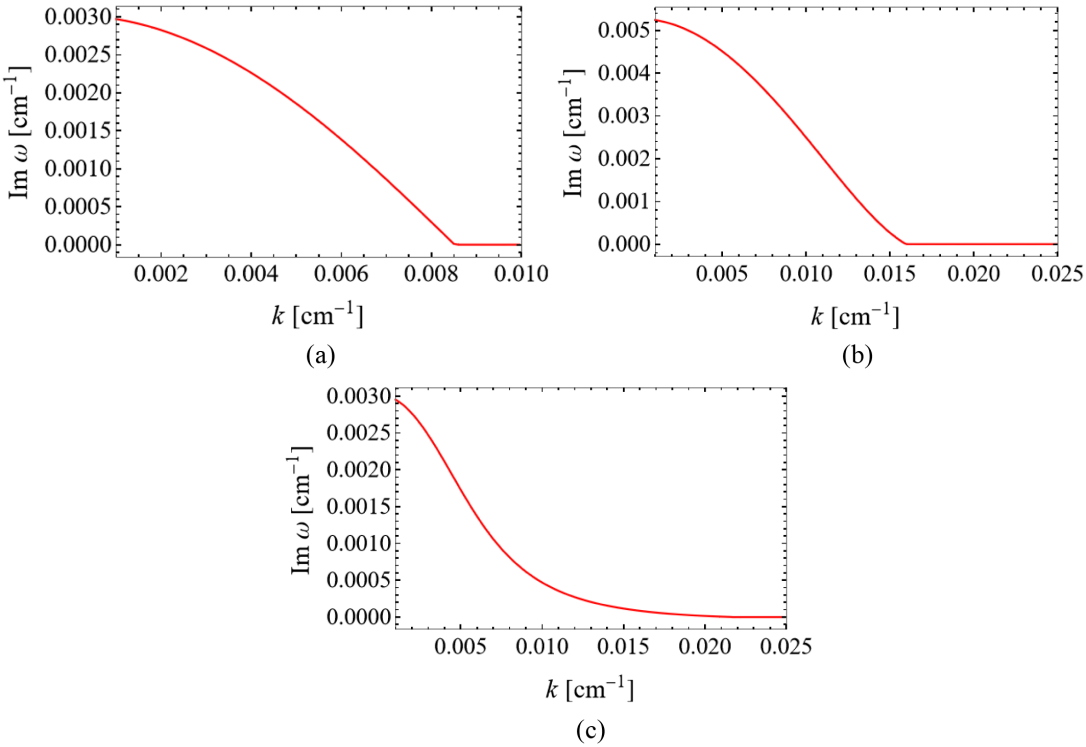

FIG. 12. The linear growth rates for the unstable branches Q in (a), W in (b), and Y in (c) as functions of the wave number k.

In Fig. 13 we plot the linear growth rates for the three modes Q, W, and Y as functions of $\bar{g}$ at $\delta = 0.4$ to show that the resonancelike structure occurs indeed also in this case. Note that Q and Y are strictly distinct from each other at $\delta \neq 0$. In Fig. 14 we demonstrate how the background anisotropy affects CFI. It is observed that it tends to reduce CFI. This time the effect is pretty minor, though.

Now we go on to the study of a possible interplay of the resonancelike phenomenon in CFI with FFC. For this purpose we choose

$$\delta = 0.1, \qquad \bar{\delta} = 0.08. \tag{60}$$

The values of other model parameters are unnchanged from the previous case for $\delta = \bar{\delta}$. We adjust $\bar{g}$ so that there should be an ELN crossing in the angular distributions of ν_e and $\bar{\nu}_e$. There is indeed an interval of $\bar{g}$, in which the angular ELN crossing and thus FFC occur. In this model, ν_e is dominant in the radially outward direction while the opposite is true in the inward direction. Note that the mean energies and collision rates for $\bar{\nu}$ are unchanged by the variation of $\bar{g}$. We study at $k = 0$ the behavior of the fast-unstable branch in the presence of the collision term.

We show in Fig. 15(a) the growth rates of this mode as functions of $\bar{g}$ both with (red) and without (blue) the collision term. As is evident from the latter, FFC occurs in this mode for $0.505 \lesssim \bar{g} \lesssim 0.517$, where Im$\omega$ is positive. Interestingly, the resonancelike structure in CFI takes place almost in the same region as could be inferred from the red line, in which the foot of the resonancelike peak can be recognized near the both ends of the FFC range. It is also apparent that the resonancelike phenomenon has a very small impact on the growth rate when the FFC is in operation: it only modifies the amplitude very slightly and shifts the peak position only a bit.

This is more evident when we take a different parameter set; $\delta = 0.1$ and $\bar{\delta} = 0.095$. The result is shown in Fig. 15(b). In this case, the degrees of anisotropy are not much different between ν_e and $\bar{\nu}_e$ and, as a consequence, the range for the ELN crossing is much narrower in $\bar{g}$ (see the blue line). Now the shift in the peak position by the resonancelike phenomenon in CFI is apparent. Note that without FFC the height and width of the resonancelike structure are essentially unchanged with this variation of $\bar{\delta}$. Because of this shift, the amplitude of FFC, on the other hand, is enhanced or reduced, depending on where we look at. Such a shift becomes also noticeable for larger deviations of $\bar{\delta}$ from δ if the difference in the collision rates is large enough. As mentioned above, it seems that when FFC and the resonancelike phenomenon in CFI are simultaneously in operation, the growth rate is set by the former (recall that the growth rate of CFI at the resonancelike peak for the current setting at $\delta = \bar{\delta}$ is ~ 0.005 cm^{-1}, i.e., 10 times smaller than the growth rate of FFI alone). More systematic investigations in a broader parameter range are certainly needed to see how generic this is, but they will be deferred to future studies.

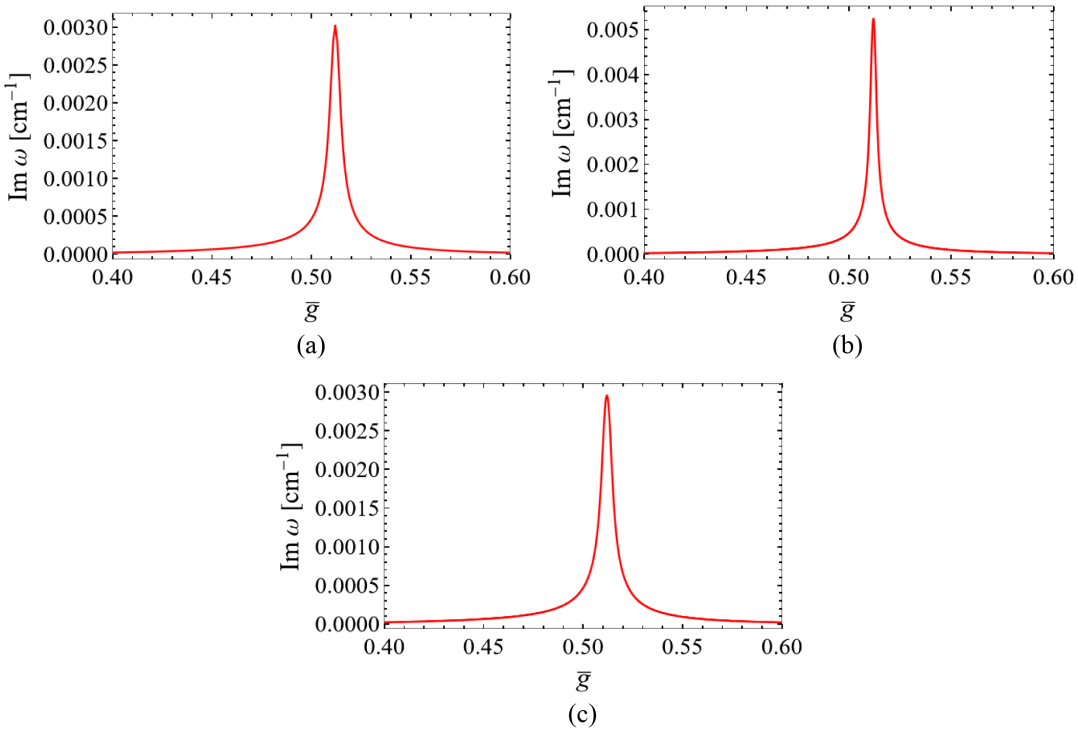

FIG. 13. The resonancelike structures for the anisotropic neutrino backgrounds. The degree of anisotropy is identical for ν_e and $\bar{\nu}_e$: $\delta = \bar{\delta} = 0.4$. (a)–(c) correspond to the unstable banches Q, W, and Y respectively. Note that Q and Y are no longer degenerate.

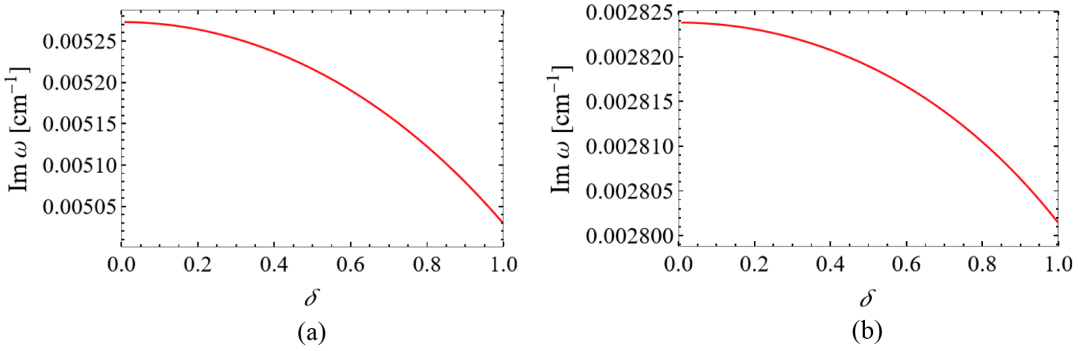

FIG. 14. The linear growth rates for mode W studied as functions of the degree of anisotropy δ. (a) at the resonancelike peak ($\bar{g} = 0.512$) and (b) at roughly half the peak amplitude ($\bar{g} = 0.51$).

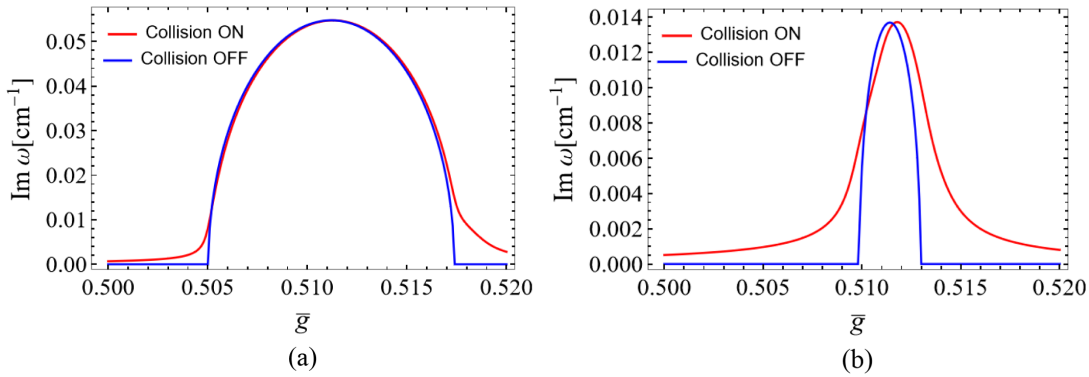

FIG. 15. The linear growth rates as functions of $\bar{g}$ for anisotropic backgrounds with an ELN crossing. The collision term is either turned on (red) or off (blue). (a) $\delta = 0.1$ and $\bar{\delta} = 0.08$ and (b) $\delta = 0.1$ and $\bar{\delta} = 0.095$.

V. CONCLUSION

We have presented in this paper the results of a systematic study on the resonancelike structure in CFI. Employing the two-flavor approximation for simplicity, we have done both linear analysis and nonlinear numerical simulations. The collision is taken into account in the relaxation approximation, which is actually exact for the emission/absorption as well as iso-energetic scatterings of neutrinos. We have always assumed that the neutrino distributions are homogeneous initially but have considered both isotropic and anisotropic distributions in momentum space. We have also taken into account the continuous energy distributions of neutrinos. By changing rather arbitrarily the number densities or the collision rates for the antineutrinos, we have produced both configurations in and out of the resonancelike region freely.

Starting with the linear analysis of the simplest case, i.e., the monochromatic, homogeneous, and isotropic background with $k = 0$ perturbations, we have analytically obtained the dispersion relations both for the isotropy-preserving and isotropy-breaking modes. Note that the latter has been overlooked in the literature so far. We have confirmed that the resonancelike structure shows up at $A \sim \alpha$ [see Eq. (21) for the notations] for the isotropy-preserving branch, where the two modes, ω_+ and ω_- [Eq. (19)], come close to each other. We have demonstrated that a similar feature occurs at $A \sim 3\alpha$ also for the isotropy-breaking branch. In both cases, the resonancelike peak is obtained at $\mathfrak{g} \sim \bar{\mathfrak{g}}$ [Eq. (17)] but not exactly at $\mathfrak{g} = \bar{\mathfrak{g}}$. In fact, the deviation becomes larger for a greater difference between the collision rates, Γ for neutrino and $\bar{\Gamma}$ for antineutrinos. The resonancelike region is also broadened in that case.

We have then conducted numerical simulations for the same background setting to investigate the nonlinear evolutions of the perturbations, which were again assumed to have $k = 0$ and added only to the off-diagonal components of the density matrix. We have confirmed the exponential growth at the rate given by the linear analysis in the linear phase, which we have found is followed by the nonlinear saturation phase, where the flavor coherence levels off and the distribution functions are settled to new steady states asymptotically. We have observed a bouncing with large amplitudes only around the resonancelike peak. Its mechanism is unclear for the moment but we have demonstrated that it is induced mainly by the diagonal part of the collision term.

We then proceeded to the nonmonochromatic case, in which we assumed that neutrinos have Fermi-Dirac distributions as their energy spectra. In the linear analysis for the homogeneous and isotropic background with the $k = 0$ perturbation, we have shown that there are again isotropy-preserving and isotropy-breaking branches and that both of them give a resonancelike structure. We also demonstrated that the growth rate in the resonancelike structures is well-approximated by the exact formula for the monochromatic case with an appropriate substitution of variables as long as the collision rates are not much different between neutrino and antineutrino. This was pointed out in the previous work [33] for small collision rates. Our results have extended its validity.

The nonlinear simulations have been done for the same background as for the linear analysis above. The perturbation was assumed to have $k = 0$ and to be also isotropic. Only the isotropy-preserving mode has been calculated. As expected from the dispersion relation, we observed that the perturbation grows exponentially at the same rate for all energies of neutrinos. We have found that for different energies of neutrinos the nonlinear saturation phase begins when their flavor coherence becomes of the similar amplitude to the distribution functions at their energies, $|S(E)| \sim f(E)$ [Eq. (1)], a direct extension of the monochromatic case. We found that the saturation level is not affected much by the resonancelike phenomenon and its main role is to shorten the time it takes to get to the saturation. We have also seen the bouncing of the flavor coherence after its peak-out near the resonancelike peak alone again.

We finally conducted the linear analysis either for the $k \neq 0$ perturbation to the isotropic background or for the $k = 0$ perturbation to anisotropic background configurations. In the former we have shown how the isotropy-preserving and isotropy-breaking branches at $k = 0$ are mixed for $k \neq 0$ to produce new branches and demonstrated that resonancelike structure occurs just in the same way for all these modes. We have also found that the CFI is weaker for modes with $k \neq 0$ than $k = 0$.

For the anisotropic background with no electron-lepton-number, or ELN, crossings, we have shown that resonancelike structure shows up again in the same way and that the CFI tends to be weaker, albeit slightly, for the anisotropic background. With an ELN crossing, on the other hand, the growth rate seems to be set by the fast-flavor conversion, or FFC, and the resonancelike phenomenon in CFI, the region of which tends to overlap with the range of FFC, shifts the peak position and broadens the range of instability. The growth rate may be enhanced or reduced, depending on the position in the unstable range.

There remain many issues to be addressed further. Not to mention, we need to extend the analysis to three flavors. The relaxation approximation should be removed to incorporate nonisoenergetic collisions. The parameter regions considered in this paper are rather limited. For instance, we have investigated a rather small k in the $k \neq 0$ perturbation although new modes with different properties may emerge for larger k. Interplays of the resonancelike phenomenon in CFI with FFC in the nonlinear phase should be studied, probably numerically. Indeed the growth of the isotropy-breaking modes may induce FFC in that phase. The mechanism of the large-amplitude

bouncing in the resonancelike peak case needs to be understood. The asymptotic state in the nonlinear saturation phase should be characterized. We are interested in what consequences, if any, the resonancelike structure in CFI may have for core-collapse supernovae and compact object mergers. In fact, the advection, which is ignored in this paper, occurs in these realistic situations and the buildup time of flavor instabilities becomes crucially important [32]. These will all be future works.

ACKNOWLEDGMENTS

J. L. thanks Taiki Morinaga for introducing this field of research to him and providing well constructed basic codes for dispersion relation analysis. This work is partially supported by Grants-in-Aid for Scientific Research (21H01083) and the Grant-in-Aid for Scientific Research on Innovative areas "Unraveling the History of the Universe and Matter Evolution with Underground Physics" (19H05811) from the Ministry of Education, Culture, Sports, Science and Technology (MEXT), Japan. M. Z. is supported by the Japan Society for Promotion of Science (JSPS) Grant-in-Aid for JSPS Fellows (Grant No. 22J00440) from the Ministry of Education, Culture, Sports, Science, and Technology (MEXT) in Japan. S. Y. is supported by Institute for Advanced Theoretical and Experimental Physics, Waseda University, and the Waseda University Grant for Special Research Projects (Project No. 2022C-140).

[1] J. Pantaleone, Dirac neutrinos in dense matter, Phys. Rev. D **46**, 510 (1992).
[2] G. Sigl and G. Raffelt, General kinetic description of relativistic mixed neutrinos, Nucl. Phys. **406**, 423 (1993).
[3] H. Duan, G. M. Fuller, and Y.-Z. Qian, Collective neutrino oscillations, Annu. Rev. Nucl. Part. Sci. **60**, 569 (2010).
[4] S. Chakraborty, R. Hansen, I. Izaguirre, and G. Raffelt, Collective neutrino flavor conversion: Recent developments, Nucl. Phys. **B908**, 366 (2016), Neutrino oscillations: Celebrating the nobel prize in physics 2015.
[5] I. Tamborra and S. Shalgar, New developments in flavor evolution of a dense neutrino gas, Annu. Rev. Nucl. Part. Sci. **71**, 165 (2021).
[6] S. Richers and M. Sen, Fast flavor transformations, arXiv:2207.03561.
[7] T. Morinaga, Fast neutrino flavor instability and neutrino flavor lepton number crossings, Phys. Rev. D **105**, L101301 (2022).
[8] S. Abbar, H. Duan, K. Sumiyoshi, T. Takiwaki, and M. C. Volpe, On the occurrence of fast neutrino flavor conversions in multidimensional supernova models, Phys. Rev. D **100**, 043004 (2019).
[9] H. Nagakura, T. Morinaga, C. Kato, and S. Yamada, Fast-pairwise collective neutrino oscillations associated with asymmetric neutrino emissions in core-collapse supernovae, Astrophys. J. **886**, 139 (2019).
[10] M. Delfan Azari, S. Yamada, T. Morinaga, H. Nagakura, S. Furusawa, A. Harada, H. Okawa, W. Iwakami, and K. Sumiyoshi, Fast collective neutrino oscillations inside the neutrino sphere in core-collapse supernovae, Phys. Rev. D **101**, 023018 (2020).
[11] S. Abbar, H. Duan, K. Sumiyoshi, T. Takiwaki, and M. C. Volpe, Fast neutrino flavor conversion modes in multidimensional core-collapse supernova models: The role of the asymmetric neutrino distributions, Phys. Rev. D **101**, 043016 (2020).
[12] T. Morinaga, H. Nagakura, C. Kato, and S. Yamada, Fast neutrino-flavor conversion in the preshock region of core-collapse supernovae, Phys. Rev. Res. **2**, 012046 (2020).
[13] R. Glas, H.-T. Janka, F. Capozzi, M. Sen, B. Dasgupta, A. Mirizzi, and G. Sigl, Fast neutrino flavor instability in the neutron-star convection layer of three-dimensional supernova models, Phys. Rev. D **101**, 063001 (2020).
[14] S. Abbar, Searching for fast neutrino flavor conversion modes in core-collapse supernova simulations, J. Cosmol. Astropart. Phys. 05 (2020) 027.
[15] F. Capozzi, S. Abbar, R. Bollig, and H.-T. Janka, Fast neutrino flavor conversions in one-dimensional core-collapse supernova models with and without muon creation, Phys. Rev. D **103**, 063013 (2021).
[16] H. Nagakura, A. Burrows, L. Johns, and G. M. Fuller, Where, when, and why: Occurrence of fast-pairwise collective neutrino oscillation in three-dimensional core-collapse supernova models, Phys. Rev. D **104**, 083025 (2021).
[17] A. Harada and H. Nagakura, Prospects of fast flavor neutrino conversion in rotating core-collapse supernovae, Astrophys. J. **924**, 109 (2022).
[18] R. Akaho, A. Harada, H. Nagakura, W. Iwakami, H. Okawa, S. Furusawa, H. Matsufuru, K. Sumiyoshi, and S. Yamada, Protoneutron star convection simulated with a new general relativistic Boltzmann neutrino radiation-hydrodynamics code, Astrophys. J. **944**, 60 (2023).
[19] J. D. Martin, J. Carlson, V. Cirigliano, and H. Duan, Fast flavor oscillations in dense neutrino media with collisions, Phys. Rev. D **103**, 063001 (2021).
[20] G. Sigl, Simulations of fast neutrino flavor conversions with interactions in inhomogeneous media, Phys. Rev. D **105**, 043005 (2022).
[21] L. Johns and H. Nagakura, Self-consistency in models of neutrino scattering and fast flavor conversion, Phys. Rev. D **106**, 043031 (2022).

[22] S. Shalgar and I. Tamborra, Change of direction in pairwise neutrino conversion physics: The effect of collisions, Phys. Rev. D **103**, 063002 (2021).
[23] C. Kato, H. Nagakura, and T. Morinaga, Neutrino transport with the Monte Carlo method. II. Quantum kinetic equations, Astrophys. J. Suppl. Ser. **257**, 55 (2021).
[24] H. Sasaki and T. Takiwaki, A detailed analysis of the dynamics of fast neutrino flavor conversions with scattering effects, Prog. Theor. Exp. Phys. **2022**, 073E01 (2022).
[25] R. S. L. Hansen, S. Shalgar, and I. Tamborra, Enhancement or damping of fast neutrino flavor conversions due to collisions, Phys. Rev. D **105**, 123003 (2022).
[26] C. Kato and H. Nagakura, Effects of energy-dependent scatterings on fast neutrino flavor conversions, Phys. Rev. D **106**, 123013 (2022).
[27] I. Padilla-Gay, I. Tamborra, and G. G. Raffelt, Neutrino fast flavor pendulum. II. Collisional damping, Phys. Rev. D **106**, 103031 (2022).
[28] F. Capozzi, B. Dasgupta, A. Mirizzi, M. Sen, and G. Sigl, Collisional Triggering of Fast Flavor Conversions of Supernova Neutrinos, Phys. Rev. Lett. **122**, 091101 (2019).
[29] L. Johns, Collisional Flavor Instabilities of Supernova Neutrinos, Phys. Rev. Lett. **130**, 191001 (2023).
[30] L. Johns and Z. Xiong, Collisional instabilities of neutrinos and their interplay with fast flavor conversion in compact objects, Phys. Rev. D **106**, 103029 (2022).
[31] Y.-C. Lin and H. Duan, Collision-induced flavor instability in dense neutrino gases with energy-dependent scattering, Phys. Rev. D **107**, 083034 (2023).
[32] Z. Xiong, M.-R. Wu, G. Martínez-Pinedo, T. Fischer, M. George, C.-Y. Lin, and L. Johns, Evolution of collisional neutrino flavor instabilities in spherically symmetric supernova models, Phys. Rev. D **107**, 083016 (2023).
[33] Z. Xiong, L. Johns, M.-R. Wu, and H. Duan, Collisional flavor instability in dense neutrino gases (2022), arXiv: 2212.03750.
[34] S. Airen, F. Capozzi, S. Chakraborty, B. Dasgupta, G. Raffelt, and T. Stirner, Normal-mode analysis for collective neutrino oscillations, J. Cosmol. Astropart. Phys. 12 (2018) 019.
[35] I. Izaguirre, G. Raffelt, and I. Tamborra, Fast Pairwise Conversion of Supernova Neutrinos: A Dispersion Relation Approach, Phys. Rev. Lett. **118**, 021101 (2017).